Technical note: Kinetically resolved volatile and redox fingerprints of geologic materials by TGA/DSC-MicroGC

Shuzhuang Wu[1,2*], Samuel L. Jaccard[2], Matthieu E. Galvez[2*]

[1]State Key Laboratory of Deep-sea Science and Intelligence Technology, Institute of Deep-sea Science and Engineering, Chinese Academy of Sciences, Sanya, China
[2]Institute of Earth Sciences, University of Lausanne, Lausanne, Switzerland

Correspondence to: Shuzhuang Wu (shuzhuangwu@gmail.com), Matthieu E. Galvez (matthieu.galvez@unil.ch)

Abstract. The biogeochemical cycles of carbon, oxygen and sulfur are fundamentally interlinked, yet quantifying their ~~speciation and~~ reactivity of these elements within complex geological matrices remains a major analytical challenge. We present a novel integrated TGA/DSC-MicroGC system that simultaneously monitors mass loss, heat flow, and evolved gas composition during controlled heating in a gas mixing furnace. This approach kinetically resolves and quantifies distinct carbon and sulfur materials~~species~~ through their ~~unique~~ thermal decomposition profiles. Furthermore, continuous monitoring of oxygen consumption provides a direct measure of a material's ~~absolute redox capacity~~ oxidability in various temperature windows, ~~yielding a kinetic~~ a redox fingerprint ~~of its reducible components~~. Validation against geochemical standards and application to sediments from the Congo Basin and Alpine Lake Cadagno (Switzerland), reveal diagenetic transitions and paleoenvironmental fluxes that are invisible to conventional bulk methods. This integrated methodology provides a mechanistic, high-resolution insight into electron-transfer processes in natural materials. This ~~opens up~~offers new avenues for probing biogeochemical cycling, redox evolution and environmental reactivity across Earth systems.

1 Introduction

The fate of carbon (C) and, sulfur (S) in sediments depends not only on their bulk concentration, but also on their molecular speciation and intrinsic reactivity (Alt and Shanks Iii, 2006; Galvez, 2020; Hayes and Waldbauer, 2006; Paytan et al., 1998). For example, the ~~oxidative weathering~~oxidation of labile biomolecules occur over~~in~~ ~~distinct~~

temperature windows distinct ~~than~~ from that of refractory C phases, such as graphite. Similarly, monosulfides displays ~~a different~~ oxidation profiles that differ ~~than a~~from those of crystalline sulfides such as pyrite ~~different activation energies~~ (Boudreau, 1992; Hemingway et al., 2018; Ordoñez et al., 2019; Sebag et al., 2016). Their combustion ~~also differs in reaction~~ enthalpy and O_2 demand differ too, reflecting the~~ir~~ specific bonding ~~strength~~ environment and redox state of each compound or mineral phase (Galvez and Jaccard, 2021). Existing analytical techniques are poorly suited to capture these key dimensions of reactivity. Standard methods, such as elemental analysis or X-ray fluorescence, quantify total C and S, but are blind to molecular speciation and oxidation behavior (Berg et al., 2022; Carter et al., 2024; Salonen, 1979; Yoon et al., 2018; Zhao et al., 2020). Meanwhile, Rock-Eval, a ~~popular~~ widely used tool in organic petrology, provides bulk chemical and kinetic parameters for hydrocarbon source rocks (Espitalie et al., 1985)~~.~~ ~~but~~However, its ~~it has critical limitations in this context. It~~ focus ises ~~s~~ primarily on the ramped pyrolysis and ~~combustion~~ oxidation of carbon-bearing materials, and only the latest ~~version~~generation, Rock-Eval 7, allows sulfur to be characterized simultaneously~~ing~~ ~~sulfur~~ (Cohen-Sadon et al., 2022). ~~However~~Moreover, Rock-Eval~~it~~ ~~cannot~~ does not directly link thermal degradation and combustion profiles to their underlying oxygen demands, which is a key parameter for quantifying the redox state and oxidation potential of rocks and sediments~~.~~ ~~.~~

Recent advances, such as the high-temperature titration method of Galvez & Jaccard (Galvez and Jaccard, 2021), have successfully quantified the total redox capacity of natural samples, partially bridging the gap between compositional and redox characterization. ~~However~~But this~~, the standard~~ protocol was designed as an endpoint measurement and, as such, ~~provides no kinetic resolution~~does not kinetically resolve ~~of~~ the oxidation process, which we ~~call~~ define here as the ‘oxidability’ of the sample: the temperature-dependent distribution of oxygen consumption, mass loss heat release ad gas production during controlled heating~~.~~ In addition, ~~it~~ the endpoint approach does not provide direct insight into the individual contributions of C, S, and redox-active iron (Fe)

species—including iron locked in mineral lattices (e.g., Fe(II) in silicates, oxides, and sulfides such as pyrite), as well as iron complexed within or adsorbed onto organic biomass— to the overall oxygen demand (~~cite~~ Galvez et al., 2025).

Consequently, a major disconnect persists between our understanding of global redox cycles and our ability to characterize the ~~kinetic heterogeneity and coupled redox behavior~~ combustion kinetics of the materials that drive them. To address this gap, an analytical approach is required that goes beyond bulk characterization, ~~but~~ provid~~es~~ing a simultaneous, kinetically -resolved view of mass loss, heat flow, oxygen consumption and gas evolution during ramped pyrolysis or combustion.

We have developed such a platform: a novel integrated system combining thermogravimetric analysis (TGA), differential scanning calorimetry (DSC), and micro gas chromatography (MicroGC). This configuration enables real-time, correlated measurements of mass loss, heat flow, and the evolving composition of gases, including ~~(e.g.,~~ O_2, CO_2, SO_2, H_2S, COS,~~)~~ throughout controlled thermal decomposition and oxidation. Specifically, this integration enables two key innovations:

1) It ~~enables the kinetic resolution and quantification~~quantifies ~~of distinct~~distinguishes thermally reactive C and S ~~species~~ pools based on their characteristic ~~thermal~~ decomposition or oxidation profiles and activation energies.
2) It ~~provides~~ measures ~~the~~ oxygen demand during~~for~~ combustion in a continuous, kinetically -resolved set-up ~~measure of oxygen demand for combustion~~ by directly monitoring oxygen consumption, yielding a unique ~~"~~chemical, thermal and redox fingerprint~~"~~ for each sample.

Together, these capabilities reveal a new means of characterizing ~~diagenetic pathways and paleoenvironmental signatures in complex natural archives that remain inaccessible to conventional analytical techniques~~redox reactivity. By linking mass loss, heat flow, gas evolution and oxygen demand ~~within a single framework~~, this

approach can reveal diagenetic pathways and ~~paleoenvrionmental~~paleoenvironmental signatures in complex natural archives that remain inaccessible to conventional bulk analytical techniques.

2 Materials and Methods

2.1 Sample selection and preparation

Sediment samples for TGA/DSC-MicroGC were obtained from archived freeze-dried material.

~~As representative samples, w~~We have analyzed a range of representative sediment materials containing C, S and hydrogen (H)-bearing compounds from contrasting depositional environments: the Congo Basin, ~~DRC~~Democratic Republic of Congo (DRC) ~~(0°51'24.095"S and 19°48'29.08"E)~~ and Lake Cadagno, Switzerland ~~(46°33'01.7"N, 8°42'44.3"E)~~. The Congo Basin hosts~~is~~ the world's largest tropical peatland complex (Crezee et al., 2022; Garcin et al., 2022). ~~Kinetic resolution of redox processes in these sediments provides novel insight into~~~~It is a natural laboratory to study~~These sediments provide a natural archive for studying organic matter degradation pathways associated with peat burial and climate-driven shifts since the Last Glacial Maximum. In contrast, Lake Cadagno, a meromictic lake in Switzerland with a permanently anoxic deep layer, is an ideal natural laboratory for studying microbial redox processes and their long-term preservation in the sedimentary record (Berg et al., 2022; Berg et al., 2025; Janssen et al., 2022; Dupeyron et al., 2025). ~~Applying our approach to these samples enables exploration of evolving speciation of C and S speciation in a rapidly changing lacustrine environment.~~ ~~Applying o~~Our approach ~~to~~illuminates ~~these contrasting samples enables exploration of~~ the evolving speciation and reactivity of C-and S-bearing phases across distinct sedimentary redox environments.

~~Sediment samples for TGA/DSC-MicroGC were obtained from archived freeze-dried material.~~

2.2 Instrumentation and ultra-fast configuration mode

We coupled a TGA/DSC 3+ (Mettler Toledo) with a MicroGC 990 (Agilent SRA Instruments) (Fig. 1) and calibrated the integrated system for precise, semi-continuous H-, ~~O,~~ C-, O- and S-bearing gases ~~analysis~~ (Fig. 3).

The TGA/DSC simultaneously monitors mass and heat flow changes as a function of temperature within a programmable continuous-flow gas-mixing furnace. The MicroGC, a~~n ultra fast~~ gas chromatograph equipped with short columns, separates, identifies, and quantifies light volatile compounds, including ~~(e.g.,~~ H_2O, O_2, CH_4, CO_2, H_2S, COS and SO_2,~~)~~ present in the evolving~~ed~~ing gas mixture. In our hybrid setup, samples are heated in a programmable furnace at 10°C min^{-1} from 100-1000°C under a controlled atmosphere~~s~~ (typically 10 mL min^{-1} N_2 and 1 mL min^{-1} O_2). A secondary oxidation furnace~~oven~~ downstream of the primary furnace, ~~is (~~maintained at temperatures between 300-800°C ~~and) ensures~~was used to promote complete oxidation of evolved volatile species across the ~~entire~~ heating ramp. All carrier gases (N_2, O_2 and He) are of ultra-high purity (> 5.8; Carbagas and Linde).

Evolved gases are transferred via a heated transfer line (80°C) to the MicroGC, equipped with Molsieve 5Å (for N_2, O_2) and PORAPLOT PPU (for CO_2, H_2S and SO_2) columns for efficient separation and quantification ~~for efficient separation and quantification~~. ~~This~~~~The~~The integrated TGA/DSC-MicroGC analytical system ~~thus~~ therefore provides simultaneous, temperature-resolved measurements of mass loss, heat flow, and gas composition enabling real-time characterization of oxidation and redox processes.

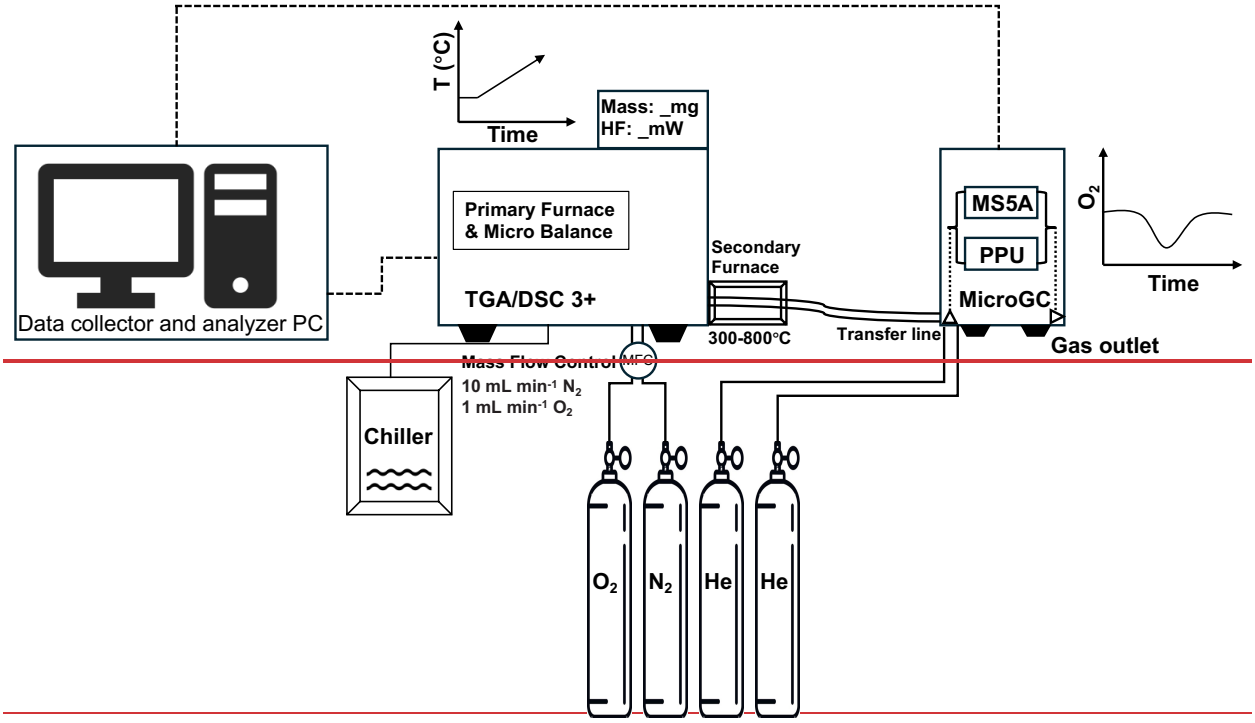
T (°C)
Time
Mass: _mg
HF: _mW
Primary Furnace
& Micro Balance
TGA/DSC 3+
Secondary
Furnace
300-800°C
Transfer line
MS5A
PPU
MicroGC
O2
Time
Gas outlet
Data collector and analyzer PC
Chiller
Mass Flow Control MFC
10 mL min-1 N2
1 mL min-1 O2
O2
N2
He
He

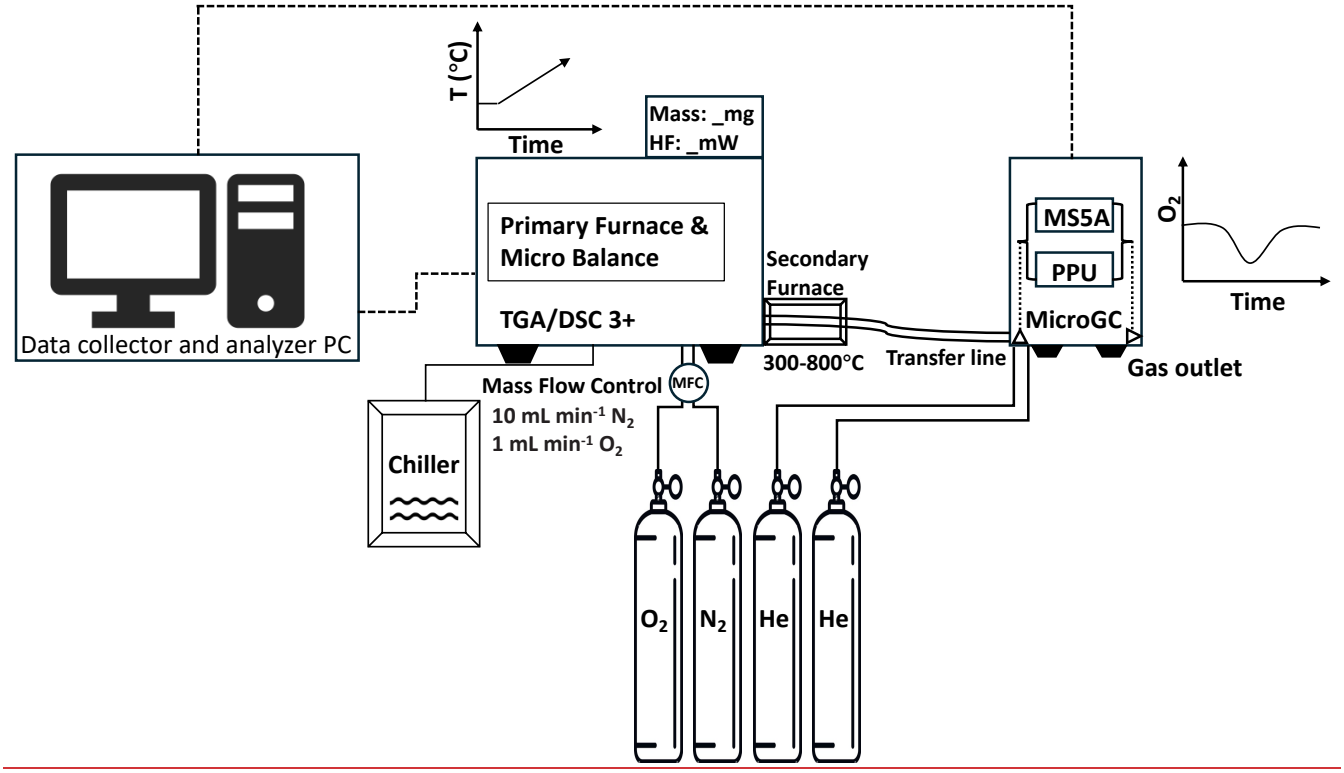

Figure 1. TGA/DSC-MicroGC instrument schematic.

2.3 Ultra-fast chromatographic mode

To resolve discrete devolatilization events, we configured our Agilent Micro GC990 ~~(~~Solia~~)~~ system for ~~a unique,~~ ultra-fast dual-channel operation with a total cycle time of 54 ~~seconde~~ s, comprising ~~(~~15 s of sampling time and 39 s of chromatographic separation ~~run~~). ~~Indeed, our target was not perfect peak separation~~The objective was not to maximize separation of light or heavy hydrocarbons~~-~~, —as is typically prioritized in chromatographic~~y in~~ cycles lasting ~~over~~ more than two minutes~~-~~, —but rather to maximize~~al~~ sampling~~point~~ density ~~to~~ and capture ~~the~~ transient devolatilization profiles of light molecules ~~with~~ at ~~high temporal~~high temporal resolution. The following ultra-fast

MicroGC configuration prioritized cycle speed while maintaining robust ~~, and also resulted in excellent~~ peak separation for the target gases.~~:~~

Channel A employed an MS5A SS column (10 m × 0.25 mm) held at 100 °C and 2.30 bar He pressure, with the injector heated at 90 °C. A ~~injector heating,~~ 15 ms injection time was used for sharp sample introduction~~,~~ and backflush was initiated~~ion~~ after 13 s of chromatography to purge retained species~~; this setup optimized rapid separation and detection~~. ~~We detect and quantify~~This setup optimized rapid separation and detection of ~~of~~ permanent gases (O_2, N_2, CO)~~ via~~using a thermal conductivity detector~~sion~~ (TCD). Channel B used a PORAPLOT U FS column (10 m × 0.32 mm) maintained at 98 °C and 2.30 bar column pressure, with the injector heated at 90 °C ~~injector.~~,~~ A~~ 50 ms injection to ensure adequate signal to noise ratio for volatile species~~s~~ at~~in~~ low concentrations~~loading of less volatile analytes~~, and backflush ~~set~~ was initiated after 10 s.~~;~~ T~~t~~his configuration enabled fast elution and quantification of CO_2, H_2S, H_2O, and SO_2.

This ~~specific~~ configuration, ~~—~~refined empirically ~~by trial and error~~through repeated optimization, ~~—~~deliver~~e~~s~~d~~ ~~one~~ a complete ~~set of~~ gas composition datapoint ~~data point~~ every 54 s. ~~It delivers, generating approximately 100 high-density data points~~devolatilization spectra ~~during over~~ A~~a~~ typical 90-minute experiment therefore generates approximately 100 high-desnity gas-evolution spectra, ~~—~~sufficient to capture transient volatile release profiles with high temporal resolution.

2.4 Data p~~P~~rocessing and kinetic parameter estimation

Raw thermogravimetric~~ams~~ and calorimetric data were initially processed using Mettler Toledo STARe software. Prior to kinetic fitting, baseline drift and buoyancy effects were corrected by subtracting blank runs performed under identical analytical conditions~~, using (empty crucibles heated alongat corresponding temperature ramps)~~.

We quantified evolved gas concentrations by external calibration against known standards and processed the MicroGC chromatograms ~~were analyzed with~~ the Solia software, which quantified ~~evolved gas concentrations via~~by external calibration against known standards~~Thermograms and calorimetric data were processed using STARe software. MicroGC chromatograms were analyzed with Solia, which quantified gas concentrations via external calibration~~ (Fig. 3 and supplementary Table S2) ~~(Fig. 3).~~.

Bulk mass-loss measurement alone does not capture the intrinsic reactivity of complex materials. To overcome this limitation, our approach uses pyrograms, heat-flow data an~~g~~d gas-evolution profiles to characterize the reaction kinetics of C and S devolatilization and/or combustion pathways based on Arrhenius-type behavior (Equation 1).

$$k = A \exp\left(-\frac{E_a}{RT}\right), \quad (1)$$

where k is the temperature-dependent rate constant, A is the empirically derived Arrhenius pre-exponential ("frequency") factor, E_a is the activation energy, R is the ideal gas constant, and T is the measured temperature (see Table 1 for symbol descriptions).

To extract ~~these~~ kinetic parameters, we employed a dual-model approach:

1) **Model-Free Isoconversional Method:** First, a~~A~~pparent activation energies (aE_a) were ~~first~~ determined using the model-free isoconversional method of Vyazovkin (Vyazovkin and Wight, 1999)~~. This was~~ implemented ~~directly~~ within the kinetics evaluation module of the STARe software. This reaction was~~,~~ evaluate~~ding~~ the ~~reaction~~ across discrete fractional conversion~~s~~ ~~segments~~intervals (α). This ~~method~~approach does not require~~s~~ prior~~no~~ assumptions about the reaction model and served as our baseline for parameter validation.

2) **Distributed Activation Energy Model (DAEM):** Second, w~~W~~e compared the isoconversional results with those obtained using a parallel-reaction Distributed Activation Energy Model (DAEM), following the methodology outlined by Hemingway et al. (2017) . A critical step in our parameterization was the

treatment of the pre-exponential factor (A). Use of~~tilizing~~ a fixed A value led to systematic overestimation~~tes led to a systematic overestimation of~~ of activation energies ~~activation energies~~ for certain ~~complex~~ standards such as calcite that do not follow a first-order decomposition kinetics (Fig. 4). Consequently, A was iteratively optimized across a boundary range of 10^5 to 10^{12} s^{-1} to ensure ~~that the aE_a values are~~consistency between DAEM~~;~~-derived apparent activation energies to those obtained ~~consistent with~~using the isoconversional method. ~~We applied~~ T~~t~~This optimized protocol was subsequently applied ~~was subsequently applied~~ to all natural samples.

3 Results

3.1 Method v~~V~~alidation: t~~T~~hermal s~~S~~ignatures and c~~C~~alibration

The integrated analytical system produces distinct thermal decomposition and combustion signatures for a range of C- and S-bearing standards, allowing ~~precise~~ robust characterization of their ~~molecular~~ thermal ~~speciation~~ reactivity and associated gas-evolution patterns (Fig. 2). Organic standards, such as L-cystine and cellulose, exhibited multi-stage decomposition profiles (Fig. 2A, B). ~~L-cystine, a sulfur-rich amino acid, decomposed primarily~~L-cystine, a sulfur-rich amino acid, decomposed primarily between 200°C and ~~700~~300°C under~~in~~ ~~pure~~ N_2/O_2 (10:1 vol:vol) mix atmosphere, releasing ~~-~~CO_2, H_2S, and COS ~~:~~(Fig. 2A, H). ~~, while~~ere ~~C~~cellulose ~~pyrolyzed~~ combusted between 250°C and ~~600~~350°C, releasing primarily CO_2 and H_2O (Fig. 2B, I). The ~~IFP~~IFPEN-160 000 (IFP) standard displays overlapping mass-loss events, ~~likely~~ reflecting the concurrent oxidation of ~~both~~ organics ~~with the~~and devolatilzation of~~and inorganic carbon phases~~carbonates (a non-redox decarbonation reaction) (Fig. 2C, J). In contrast, inorganic standards yielded sharper~~er~~ and more ~~more~~ distinct thermal spectra. Calcium carbonate ($CaCO_3$), for instance, exhibited a single, well-defined ~~44%~~ mass loss of ~44% between 600°C and 800°C, consistent with its thermal decomposition into CaO and CO_2 (Fig. 2D, K).

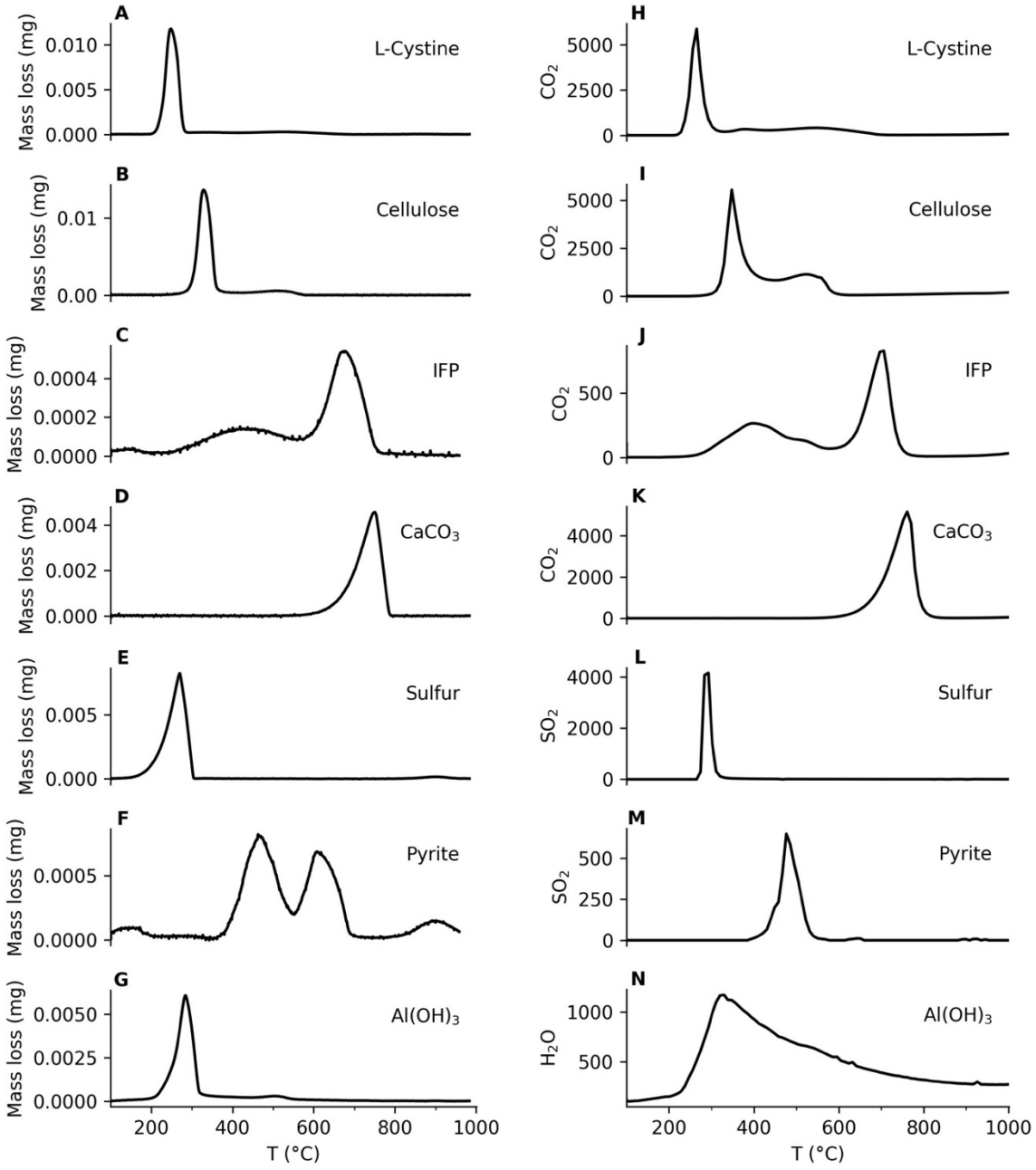
A
L-Cystine
Mass loss (mg)
0.010
0.005
0.000
B
Cellulose
Mass loss (mg)
0.01
0.00
C
IFP
Mass loss (mg)
0.0004
0.0002
0.0000
D
CaCO3
Mass loss (mg)
0.004
0.002
0.000
E
Sulfur
Mass loss (mg)
0.005
0.000
F
Pyrite
Mass loss (mg)
0.0005
0.0000
G
Al(OH)3
Mass loss (mg)
0.0050
0.0025
0.0000
200
400
600
800
1000
T (°C)
H
L-Cystine
CO2
5000
2500
0
I
Cellulose
CO2
5000
2500
0
J
IFP
CO2
500
0
K
CaCO3
CO2
4000
2000
0
L
Sulfur
SO2
4000
2000
0
M
Pyrite
SO2
500
250
0
N
Al(OH)3
H2O
1000
500
200
400
600
800
1000
T (°C)

190

Figure 2. Mass loss and devolatilized components from standards evaluated by using TGA/DSC-MicroGC system. (**A, H**) L-Cystine; (**B, I**) Cellulose; (**C, J**) IFP; (**D, K**) $CaCO_3$; (**E, L**) Elemental sulfur; (**F, M**) Pyrite; (**G, N**) $Al(OH)_3$.

Elemental S underwent rapid volatilization ~~and accompani~~followed by partial oxidation to SO_2 between 100°C and 300°C under ~~both non-oxidative and~~ oxidative condition~~s~~ (Fig. 2E, L). In contrast, pure pyrite (FeS_2) showed a distinct oxidative mass loss between 400°C and 600°C, corresponding to its conversion to Fe_2O_3 and release of SO_2 (Fig. 2F, M). Aluminium hydroxide [$Al(OH)_3$] released structural water (~13% mass loss) between 200°C and 300°C as it dehydrated to Al_2O_3 (Fig. 2G, N). The combined TGA/DSC-MicroGC profiles thus differentiate organic from inorganic C~~-profiles thus allow differentiation between organic and inorganic C and between organic~~ and ~~inorganic~~ S-bearing species~~,~~ based on their unique thermal decomposition kinetics or oxidation behaviour and ~~characteristic~~ diagnostic gas-phase reaction products. This ~~capability provides a~~ kinetically resolved ~~and reactivity-resolved molecularly specific view of insight~~information ~~redox-active phases, an analytical resolution that~~ is not ~~achievable~~ accessible with conventional bulk characterization techniques.

We ~~This~~ operated the hybrid system ~~can also be operated~~ in oxidation mode, enabling accurate quantitative ~~determiantions~~determinations~~fication~~ of ~~total~~ H-, C- and S-bearing volatile production ~~concentrations~~and thereby allowing estimation of the corresponding reactive H, C and S contents. Under these conditions, ~~all~~ reactive H-, C-, S-bearing species are completely oxidized to H_2O, CO_2 and SO_2, respectively, allowing ~~for~~ direct ~~measurement~~ quantification ~~of total element content~~from gas-evolution signals. ~~We calibrated~~ H_2O was calibrated by dehydrating $Al(OH)_3$ under controlled conditions ~~H_2O calibration was achieved through controlled dehydration of [$Al(OH)_3$], which releases a stoichiometric amount of water~~ (Fig. 3A). CO_2 calibration was performed using multiple certified reference materials to ensure accuracy and linearity across diverse matrices and CO_2 generation mechanisms. Synthetic vitreous carbon, natural graphite, and the IFP standard were combusted in oxidation mode;

pure $CaCO_3$ was thermally decomposed to release structural carbonate CO_2; and ambient air (427 ppm CO_2) served as an independent gas-phase standard (Fig. 3B). ~~We used certified reference materials to c~~Calibrateion for ~~CO_2 was calibrated using employed certified reference materials, includingcertified reference material, including industrial synthetic vitreous carbon and natural graphite, which . They, which were combusted in the oxidation mode to produce CO_2, and as well as pure calcium carbonate ($CaCO_3$), which decomposed into its constituents (Fig. 3B) CaO and CO_2. Additional calibration checks used ambient air with a known CO_2 concentration (427 ppm) and an IFP standard (Fig. 3B).~~ ~~We calibrated~~ Calibration for Sulfur species were calibrated ~~was performed~~ using the oxidation of pyrite, IFP, CLB_1 and JSD_1 standards, yielding ~~a~~ well~~-~~ defined SO_2 peaks (Fig. 3C). The resulting calibration curves for H_2O, CO_2 and SO_2 exhibit excellent linearity (R^2 >0.99~~, Fig. 3~~), confirming the robustness and precision of quantitative measurements ~~under~~ in oxidation mode (Fig. 3).

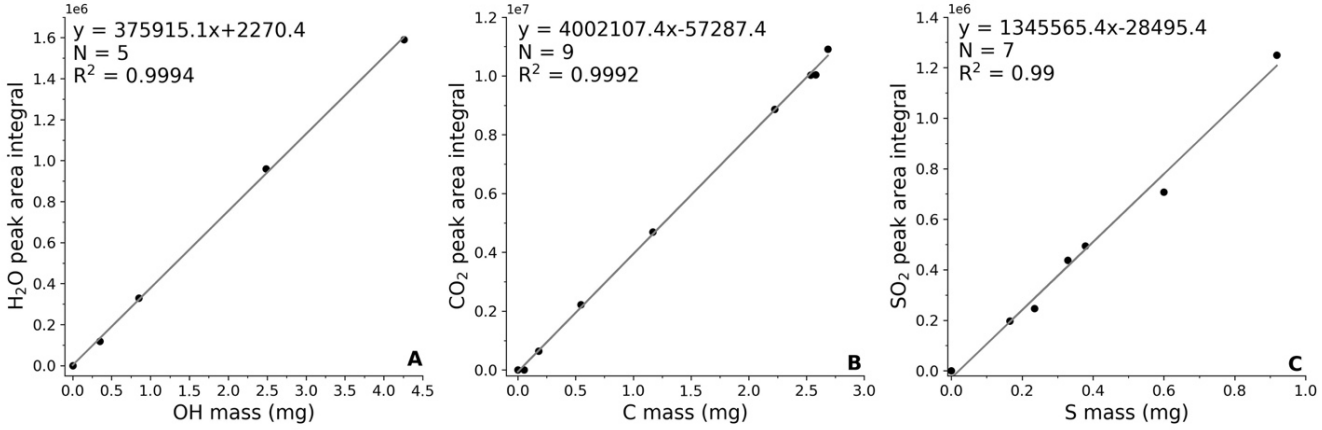

Figure 3. Gas concentration calibrations~~Calibrations~~**. A,** Hydrogen; **B,** Carbon; **C,** Sulfur. Note: The different mass ranges for H, C and S calibration due to our calibrations focus on the typical ranges of H, C, S concentrations in the natural samples. S is typically low, while H and C can reach much higher concentrations in rocks and sediments, so the calibration reflects this wider range (see supplementary Table S2). The different slopes are

reflecting different behaviors of the elements and response of the sensor~~x-axis ranges differ between panels due to element-specific stoichiometry and differences in MicroGC detector sensitivity for each analyte~~.

3.2 Kinetically-resolved c~~C~~haracterization of c~~C~~arbon and s~~S~~ulfur in n~~N~~atural s~~S~~amples

To test the kinetic approach, we first analyzed $CaCO_3$ (99.9 % purity) using the model-free isoconversional method (Fig. 4A-D). The method yielded a reaction enthalpy (ΔH) of 177 kJ mol^{-1} and aE_a of 164 kJ mol^{-1}, both consistent with published values (L'vov, 1997). In contrast, the DAEM with a fixed pre-exponential factor (A = 10^{10} s^{-1}) produced an overestimated aE_a of ~250 kJ mol^{-1}. Adjusting A to $10^{5.5}$ s^{-1} resulted in a~~the~~ aE_a of~~to~~ 162 kJ mol^{-1}, closely matching the isoconversional estimate and literature values (Fig. 4D). Applying this~~e sample~~ approach to a natural sediment ~~sample~~ from the Congo Basin (Fig. 4E-H) revealed two distinct modes with~~at~~ aE_a =~~at~~ 160 kJ mol^{-1} and 120 kJ mol^{-1}, respectively. These~~is~~ modes are~~is~~ consistent with a ~~two~~multi-step decomposition process ~~likely of distinct~~involving ~~different labile and refractory organic matter fractions~~organic matter fraxtions with contrasting thermal reactivity. The DAEM with fixed A = 10^{10} s^{-1} again overestimated activation energies (~180 kJ mol^{-1} and 140 kJ mol^{-1}), ~~while~~whereas an optimized ~~optimization to a~~ prefactor of A = $10^{8.5}$ s^{-1} ~~yielded~~produced values comparable to the isoconversional results. These results ~~confirm~~demonstrate that ~~dynamic adjustment of~~ the ~~prefactor~~pre-exponential factor is not a universal constant across mineral and sedimentary matrices, but depends on sample structure, crystallinity,~~ie. on~~ reaction pathway and the nature of the reacting phase~~A is critical for~~ . ~~This requires accurately~~Ceareful parametrization is therefore required~~ing the heterogeneous natural materials~~, particularly for natural~~in~~ samples ~~those~~ containing mixed organic and mineral phases.

~~3.2~~

~~Bulk mass-loss measurement alone does not capture the intrinsic reactivity of complex materials. To overcome this limitation, our approach uses pyrograms as a direct measure of the kinetics of C and S devolatilization and/or combustion pathways following Arrhenius law (Equation 1).~~

~~$k = A \exp\left(-\frac{Ea}{RT}\right)$, (1)~~

~~where k is the temperature dependent rate constant, A is the empirically derived Arrhenius pre exponential ("frequency") factor, E_a is the activation energy, R is the ideal gas constant, and T is the measured temperature (see Table 1 for symbol descriptions).~~

~~Apparent activation energy (aE_a) were determined using a model free isoconversional method of Vyazovkin (Vyazovkin and Wight, 1999), implemented in the STARe software. We compared the results with those obtained using a distributed activation energy model (DAEM) following (Hemingway et al., 2017). The pre-exponential factor was iteratively optimized (10^5 to 10^{12} s^{-1}) to ensure consistency between both methods, as a fixed A values led to systematic overestimation for certain standards (Fig. 4D, H). This optimized protocol was subsequently applied to natural samples.~~

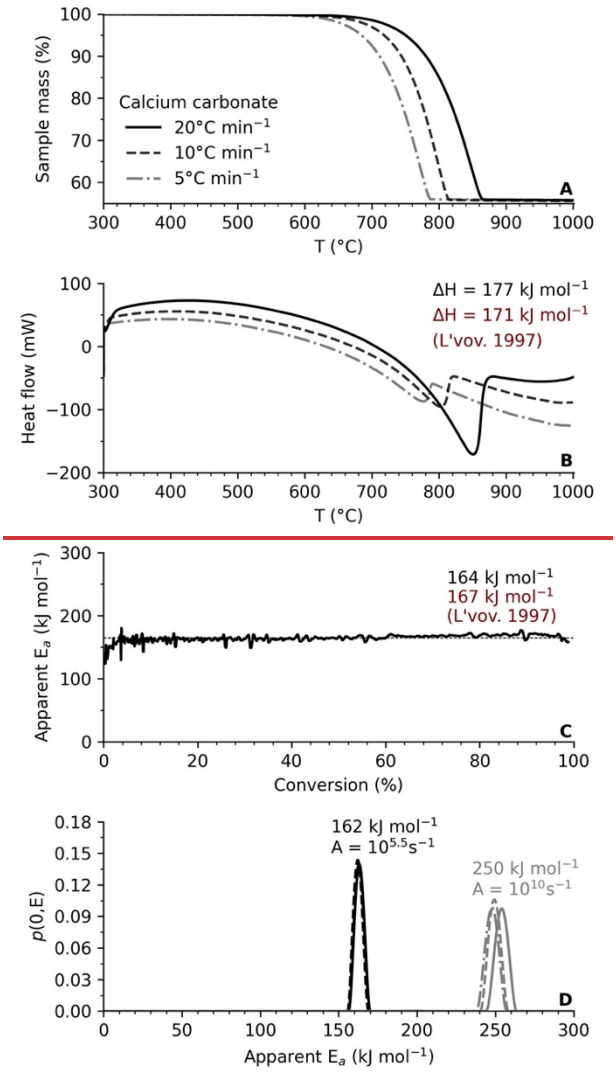
Sample mass (%)
Calcium carbonate
20°C min−1
10°C min−1
5°C min−1
A
T (°C)
Heat flow (mW)
ΔH = 177 kJ mol−1
ΔH = 171 kJ mol−1
(L'vov. 1997)
B
T (°C)
Apparent Ea (kJ mol−1)
164 kJ mol−1
167 kJ mol−1
(L'vov. 1997)
C
Conversion (%)
p(0,E)
162 kJ mol−1
A = 10^5.5 s−1
250 kJ mol−1
A = 10^10 s−1
D
Apparent Ea (kJ mol−1)

265

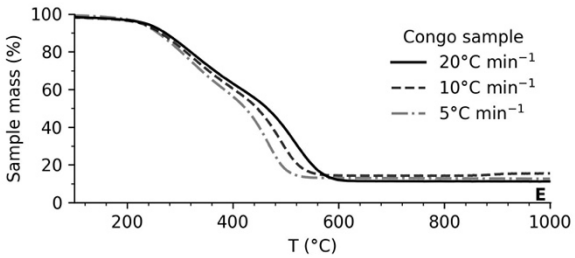
Congo sample
20°C min⁻¹
10°C min⁻¹
5°C min⁻¹
Sample mass (%)
T (°C)
E

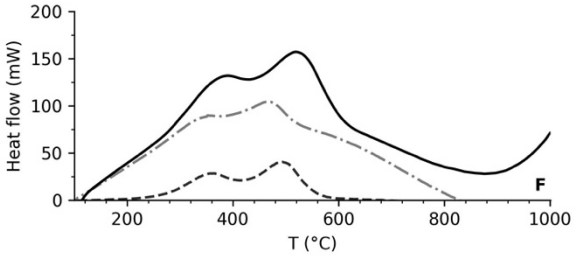
Heat flow (mW)
T (°C)
F

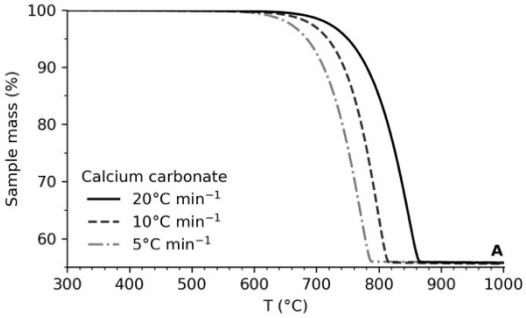
Calcium carbonate
20°C min⁻¹
10°C min⁻¹
5°C min⁻¹
Sample mass (%)
T (°C)
A

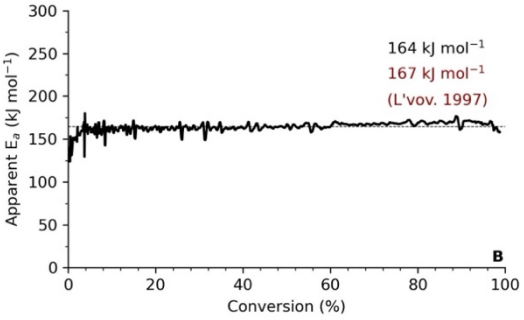
164 kJ mol⁻¹
167 kJ mol⁻¹
(L'vov. 1997)
Apparent Eₐ (kJ mol⁻¹)
Conversion (%)
B

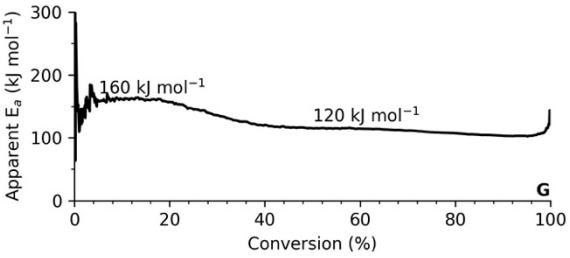
160 kJ mol⁻¹
120 kJ mol⁻¹
Apparent Eₐ (kJ mol⁻¹)
Conversion (%)
G

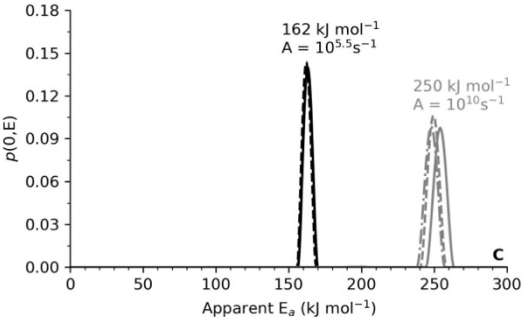
162 kJ mol⁻¹
A = 10^5.5 s⁻¹
250 kJ mol⁻¹
A = 10^10 s⁻¹
p(0,E)
Apparent Eₐ (kJ mol⁻¹)
C

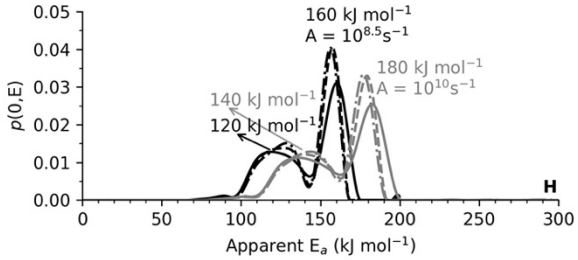
160 kJ mol⁻¹
A = 10^8.5 s⁻¹
180 kJ mol⁻¹
A = 10^10 s⁻¹
140 kJ mol⁻¹
120 kJ mol⁻¹
p(0,E)
Apparent Eₐ (kJ mol⁻¹)
H

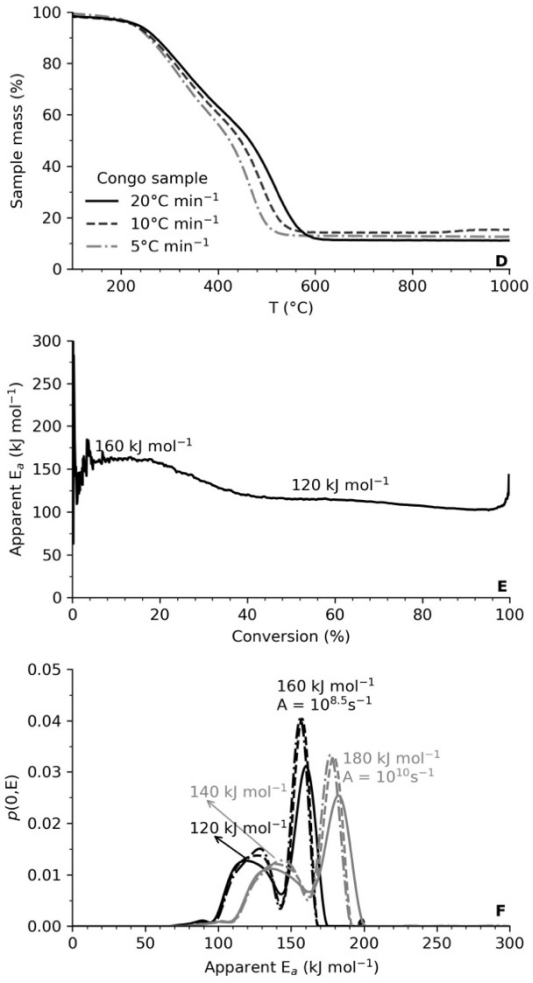

Figure 4. Thermal properties for standard calcium carbonate (left) and natural sample from Congo basin (right). (**A,** ~~**E**~~**D**) Mass loss curves from thermogravimetric analysis (TGA) at heating rates of 5, 10, and 20°C min^{-1}; ~~**(B, F) Corresponding heat flow profiles from differential scanning calorimetry (DSC);**~~ (~~**C**~~**B**~~**,**~~ , ~~**G**~~**E**) Apparent activation energy (aE_a) as a function of conversion determined via the model-free isoconversional method (Vyazovkin and Wight, 1999); (~~**D**~~**C, F,** ~~**H**~~) We derive the a~~A~~pparent activation energy distribution p(0,E) ~~derived~~

from the distributed activation energy model (DAEM) for various pre-exponential factors (A) following (Hemingway et al., 2017).

~~To test the kinetic approach, we first analyzed $CaCO_3$ (99.9% purity) using the model-free isoconversional method (Fig. 4A-D). The method yielded a reaction enthalpy (ΔH) of 177 kJ mol^{-1} and aE_a of 164 kJ mol^{-1}, both consistent with published values(L'vov, 1997). In contrast, the DAEM with a fixed pre-exponential factor ($A = 10^{10}$ s^{-1}) produced an overestimated aE_a of ~250 kJ mol^{-1}. Adjusting A to $10^{5.5}$ s^{-1} resulted the aE_a to 162 kJ mol^{-1}, closely matching the isoconversional and literature values (Fig. 4D). Applying the sample approach to a natural sediment sample from the Congo Basin (Fig. 4E-H) revealed two distinct aE_a at 160 kJ mol^{-1} and 120 kJ mol^{-1}, consistent with a two-step decomposition process likely reflecting different organic matter fractions. The DAEM with fixed $A = 10^{10}$ s^{-1} again overestimated activation energies (~180 kJ mol^{-1} and 140 kJ mol^{-1}), while optimization to $A = 10^{8.5}$ s^{-1} yielded values comparable to the isoconversional results. These confirm that dynamic adjustment of A is critical for accurately parametrizing the heterogeneous natural materials, particularly those containing mixed organic and mineral phases.~~

Thermograms of peatland sediment from the Congo Basin reveal two predominant organic fractions: a thermally labile component (L) with a decomposition peak near 370°C and an aE_a of ~120 kJ mol^{-1}, and a more refractory fraction (R), ~~likely composed of aged lignocellulosic aromatic compounds~~consistent with more aromatic, thermally stable organic matter, peaking at 500°C with an aE_a of ~160 kJ mol^{-1} (Fig. 5A). The ratio of the labile-to-refractory peak areas (L/R) increases markedly following peat initiation, indicating a higher proportion of thermally labile organic material. This substantial increase suggests either a shift in organic matter sources and/or enhanced preservation of labile compounds within the peat profile. This interpretation would be consistent with

independent paleoenvironmental proxies that ~~pointing~~ point to a transition to wetter conditions that promoted peat accumulation and selective preservation of labile organic matter (Garcin et al., 2022).

Similarly, thermograms from Lake Cadagno sediments reveal three distinct ~~sulfur~~ S-bearing fractions. Hydrogen sulfide (H_2S) and carbonyl sulfide (COS) evolved at relatively low temperatures, with aE_a values of approximately 110 kJ mol^{-1} ~~-~~and 130 kJ mol^{-1}, respectively. This behaviour is consistent with the decomposition of labile organic sulfur compounds, such as thiols, sulfides, and disulfides associated with fresh ~~-~~organic matter (Fig. 5B). A higher temperature SO_2 peak with an aE_a value of approximately 150 kJ mol^{-1} reflects the oxidative decomposition of pyrite ~~(FeS_2)~~. This differentiation clearly separates low-temperature organic S-bearing~~sulfur compounds~~ pools from more thermally stable inorganic sulfide minerals~~, a resolution not achievable by conventional methods~~.

The low-temperature release of H_2S and COS reflects ~~consistent with~~ partial sulfurization associated with ~~provides a kinetic fingerprint of~~ dissimilatory sulfate reduction (DSR), the dominant anaerobic microbial pathway for S cycling in the lake's euxinic bottom waters. Conversely, the higher-temperature SO_2 peak reflects the thermal stability of pyrite, the end product of long-term biological ~~DSR~~ sulphate reduction and diagenetic mineralization. Together, these results demonstrate that the TGA/DSC-MicroGC approach yields quantitative, kinetically resolved signatures of microbial sulfur cycling and ~~geochemically mediated S transformations~~organic matter transformation, linking molecular-scale reactivity to environmental processes.

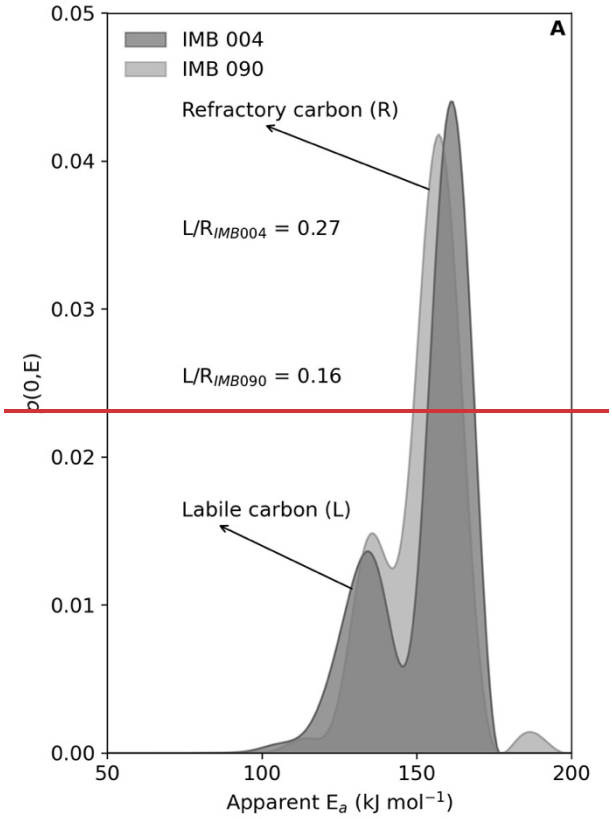
A
IMB 004
IMB 090
Refractory carbon (R)
L/R$_{IMB004}$ = 0.27
L/R$_{IMB090}$ = 0.16
Labile carbon (L)
p(0,E)
0.05
0.04
0.03
0.02
0.01
0.00
50
100
150
200
Apparent E$_a$ (kJ mol^{-1})

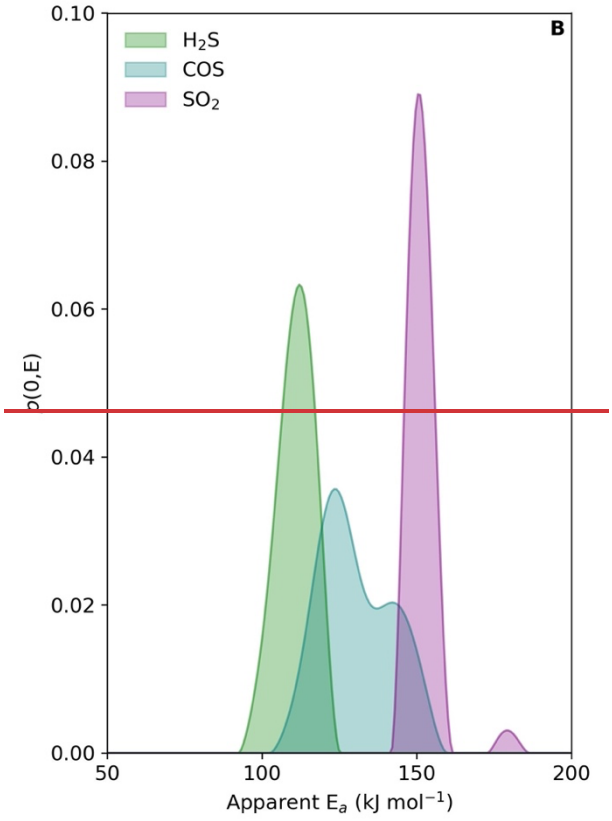
B
H_2S
COS
SO_2
0.10
0.08
0.06
0.04
0.02
0.00
p(0,E)
50
100
150
200
Apparent E_a (kJ mol^{-1})

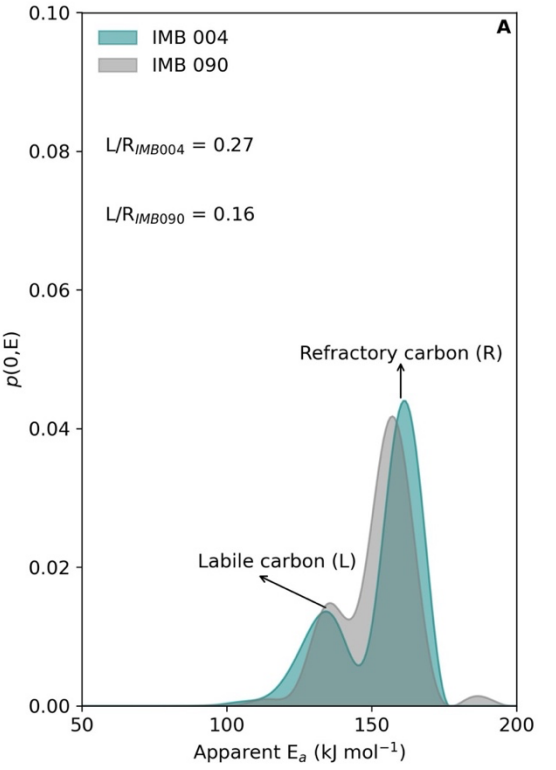
A
IMB 004
IMB 090
L/R_{IMB004} = 0.27
L/R_{IMB090} = 0.16
Refractory carbon (R)
Labile carbon (L)
0.10
0.08
0.06
0.04
0.02
0.00
p(0,E)
50
100
150
200
Apparent E_a (kJ mol^{-1})

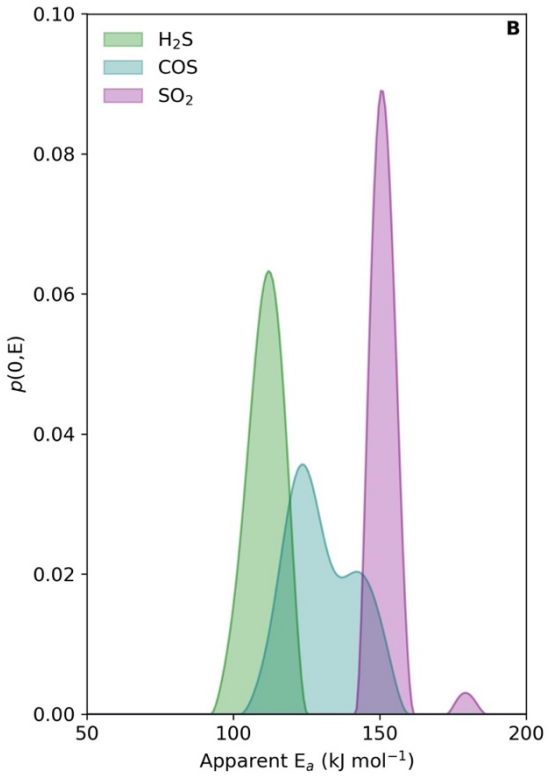

Figure 5. Kinetically-resolved carbon and sulfur speciation. A, aE_a distributions for carbon speciation in peat samples from the Congo Basin, including labile and refractory carbon fractions. **B**, aE_a distributions of sulfur speciation in a sample from Lake Cadagno ~~Lake~~, including H_2S, COS, and SO_2.

3.3 Absolute Redox Capacity and Oxidation Profiles

Having established the capacity to kinetically resolve individual species, we next address a more integrated property: ~~–~~the specific redox capacity, ~~(~~dO_2~~)~~. To move beyond thermodynamic proxies and bulk speciation, we developed a method to quantify the oxygen demand during~~on~~ combustion ~~per gram of sample~~, ~~,~~ ~~dO_2~~ , through ~~real-~~time-resolved monitoring of oxygen consumption during ~~ramping~~a controlled heating ramp~~heating~~. Previous work

havehas introduced a high-temperature chalcometric technique, which determined thes total redox capacity by measuring the total oxygen exchangged between a solid-state oxygen donor and the sample at elevated T and under vacuum (Galvez and Jaccard, 2021; Galvez et al., 2020). Although But highly effective for quantifying total oxygen demand, this earlier approach is limited to endpoint measurements. Therefore It therefore, it and does not resolve the combustionprovides no kineties resolution and cannot distinguish the individualtemperature-dependent contribution of each element-specific contributions element todifferent reactive pools to the total redox capacityto overall redox behavior.

Our method overcomes these limitations by continuously measuring O_2 concentrations in situat high temporal resoltuionresolution during the heating ramp. Samples are heated at a controlled rate (e.g. 10 °C min^{-1}), under a specific gas mixture, inducing progressive devolatilization and oxidation while the MicroGC continuously monitors the evolving gas compositions. The decline in the O_2 concentrations is integrated over time to calculate the cumulative volume of O_2 consumed, which is then normalized to the initial sample mass and the evaluated relative to the stoichiometric oxidation reactions of the major gas-producing components (Fig. 6A). This methodapproach measuresyields an absolute redox capacity with high reproducibilityoxygen demand while simultaneously preserving the temperature-resolved oxidation profile. It therefore provides both the toal redox capacity and the distribution of that capacity across distinct thermal domainsThis method yields highly reproducible measurements of absolute redox capacity. The method shows high reproductivity, , ie. with with a relative standard deviation of 0.82% for vitreous carbon standards (Fig. 6B). Importantly, our results accurately reproducesare consistent with those obtained by the vacuum line protocol (Galvez and Jaccard, 2021), validating the precision and robustness of this continuous, kinetically resolved redox quantification method.

Redox capacity (dO_2) was calculated as:

i. Volume of O_2 supply (V_{sup})

$$V_{sup} = f \times \Delta t,$$

(2)

where f is the O_2 flow rate (1 ml min^{-1}) and Δt is time interval.

ii. Volume of O_2 consumed (V_{con})

$$V_{con} = \frac{\int_{t1}^{t2} A_{eff}\, dt}{\int_{t1}^{t2} A_{tot}\, dt} \times V_{sup}\,, \quad (3)$$

where A_{eff} is time-integrated effective area corresponding to consumed O_2 and A_{tot} is time-integrated total area.

iii. Redox capacity (dO_2)

$$dO_2 = \frac{PV_{con}}{RT \times m}, \quad (4)$$

where P is gas pressure, R is the ideal gas constant, T is the room temperature and m ~~indicates~~ is sample mass.

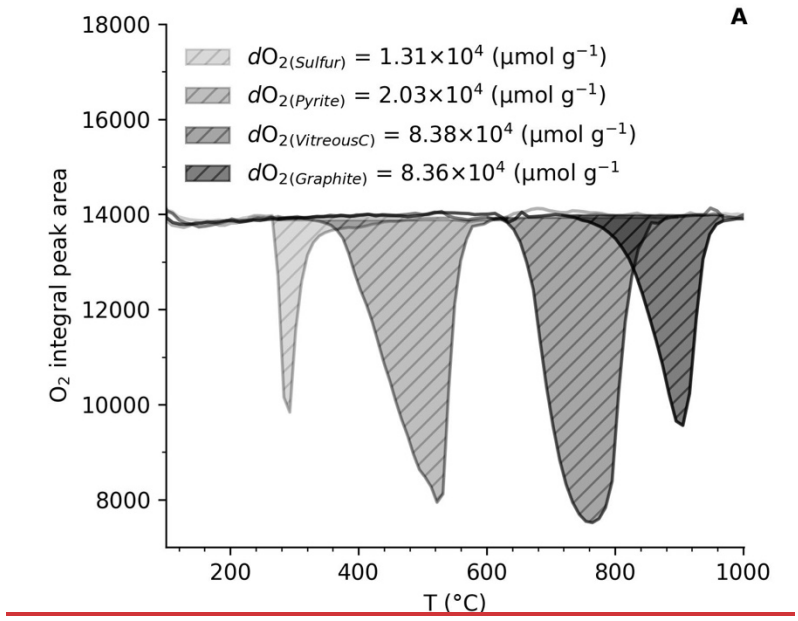
A
$dO_{2(Sulfur)}$ = 1.31×10^4 (µmol g^{-1})
$dO_{2(Pyrite)}$ = 2.03×10^4 (µmol g^{-1})
$dO_{2(VitreousC)}$ = 8.38×10^4 (µmol g^{-1})
$dO_{2(Graphite)}$ = 8.36×10^4 (µmol g^{-1}
O_2 integral peak area
T (°C)

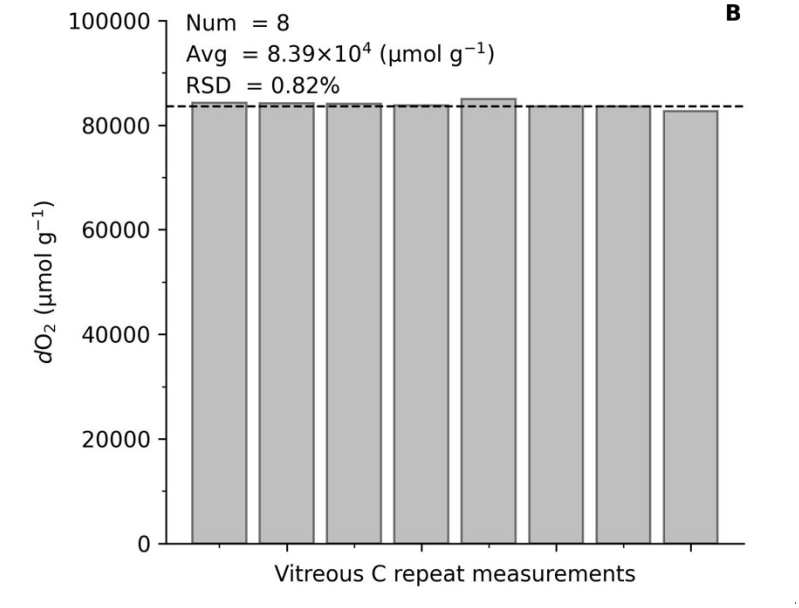
B
Num = 8
Avg = 8.39×10^4 (µmol g^{-1})
RSD = 0.82%
dO_2 (µmol g^{-1})
Vitreous C repeat measurements

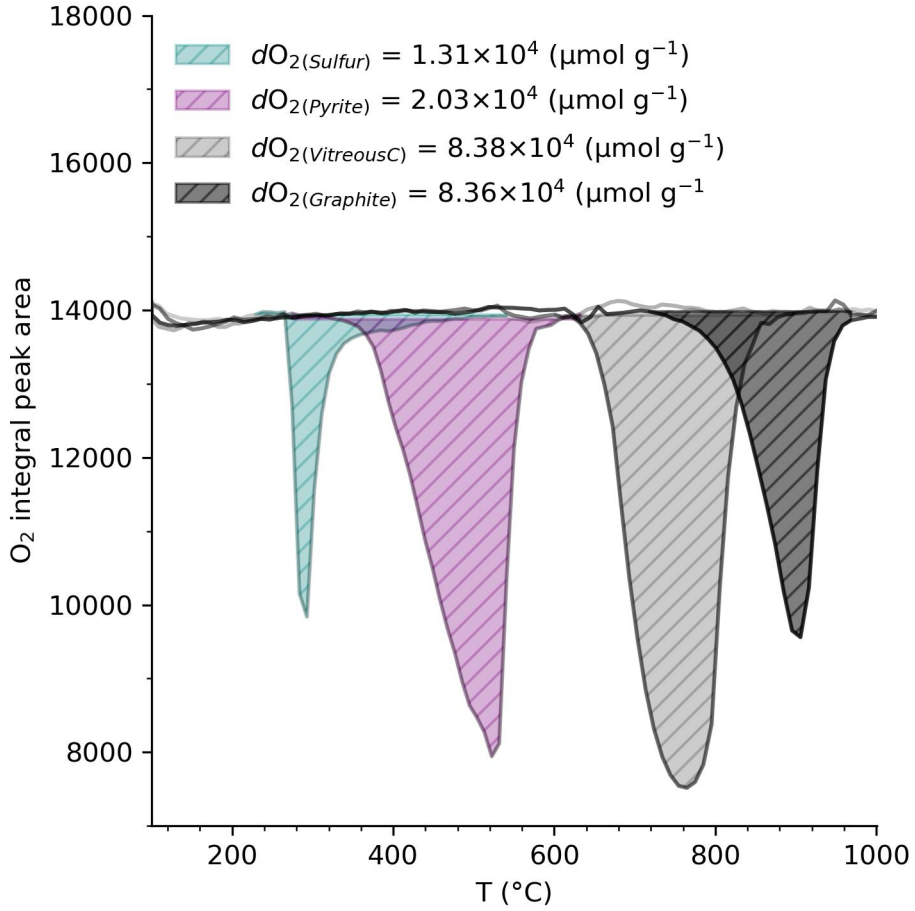

Figure 6. ~~**Redox capacity. A,**~~ **Oxygen** consumption **profiles of** elemental **sulfur, pyrite, Vitreous C and graphite** ~~**along with temperature**~~during controlled thermal oxidation. ~~**; B, Repeat measurements for standand Vitreous C with relative standard deviation (RSD = 0.82%), indicating high precision and reproducibility. Black dashed lines indicate the theoretical value.**~~

The oxidation of various standards was examined to validate this new ~~continuous~~ time-resolved dO_2 protocol. The measured dO_2 value~~s for elemental sulfur (dO_2 = 1.31 × 10⁴ μmol g⁻¹) and~~for pyrite (dO_2 = 2.03 × 10⁴ μmol g^{-1}) ~~are~~ is approximately ~~40% and~~ 11% lower~~, respectively,~~ than ~~their~~ its theoretical values (3.13 × 10⁴ and 2.29 × 10⁴ μmol g^{-1}). ~~We attribute these discrepancies to premature, non-oxidative S volatilization during heating, which prevents complete oxidation within the experimental timeframe.~~ In contrast, elemental sulfur a dO_2 = 1.31 × 10⁴ μmol g^{-1} corresponding to only ~42% of ist theoretical value (3.12 × 10⁴ μmol g^{-1}). This substantial under-recovery indicated that low-temperature volatilization can remove reactive sulfur tom the system before complete oxidation. ~~both~~ By contrast, vitreous carbon (dO_2 = 8.38 × 10⁴ μmol g^{-1}) and natural graphite (8.36 × 10⁴ μmol g^{-1}) display excellent alignment with the theoretical prediction~~s~~ (8.36 × 10⁴ μmol g^{-1}). Their oxidation occurs at higher temperatures (>400°C), where losses due to non-oxidative volatilization are minimal, confirming ~~the method's~~ precision and ~~quantitative~~ accuracy of the method for refractory ~~minerals~~phases.

~~A significant advantage of this novel method is that it quantifies the absolute redox capacity of a material independent of its current environmental redox history~~condition. ~~By~~ ~~continuously~~ tracking ~~oxygen~~ O_2 consumption throughout controlled heating, the method captures the ~~total reducible~~ cumulative amount~~inventory~~ of ~~reductants in~~reduced material that oxidized under imposed analytical conditions~~ a sample, the cumulative amount of material capable of electron exchange when exposed to an oxygen rich atmosphere~~ (Fig. 6). The integrated O_2 consumption across the ~~entire~~ full temperature range thus provides a ~~comprehensive~~ quantitative measure of intrinsic redox capacity, ~~reflecting a fundamental property of the material rather than a transient environmental state~~while the temperature-resolved profile reveals hoe this capacity is distributed among reactive pools with distinct thermal behavior.

3.4 Secondary oven and optimization of~~to~~ complete oxidation

To address the incomplete oxidation of volatile S and light hydrocarbon species, we introduced a secondary oven downstream of the primary heating chamber (Fig. 1). The oven is held at a constant, adjustable temperature (300-800°C), ~~ensuring~~ allowing ~~that~~ volatile intermediates (e.g., S vapor, reduced hydrocarbons) released at T < ~300 °C to ~~,~~remain in the gas stream long enough to undergo near-complete oxidation (Fig. 7A). This configuration reduces ~~independent of the upstream heating rate and temperature~~losses caused by low-temperature volatilization and improves recovery of reactive volatile species independently of their release temperature in the primary furnace. Measurements on standards including elemental S and pyrite confirm that the secondary oven significantly improve the oxidation efficiency (Fig. 7B, C). For instance, the measured dO_2 of pyrite increases from 2.03×10^4 μmol g^{-1} (without secondary oven) to 2.28×10^4 μmol g^{-1}~~,~~ when the secondary oven was maintained at 800°C, corresponding to 95–99% of theoretical oxidation capacity (Fig. 7C). Similarly, elemental S and other S-bearing standards displayed consistent increases in dO_2 with rising secondary oven temperatures (Fig. 7B). Natural samples from the black shales, ~~peat sediments in~~ Congo Basin peat samples and Lake Cadagno sediments~~, and Congo peat~~ also showed systematic dO_2 increases of 10–20% with ~~an 800°C~~a secondary oven held at 800°C (Fig. 7D-F). These results ~~underscore~~ highlight the important ~~critical~~ role of a secondary furnace ~~secondary heating to account for~~in minimizing ~~in mitigating~~ the low-temperature volatilization losses, particularly for labile sulfur- and fresh organic-rich materials. ~~The implementation of a secondary oven thus even better substantially improves oxidation completeness ensures quantitative oxidation of volatile phases and~~ The secondary oven improves both~~It also enhances~~ the accuracy and reproducibility of redox capacity measurements by ensuring more complete oxidation of volative ration intermediates.

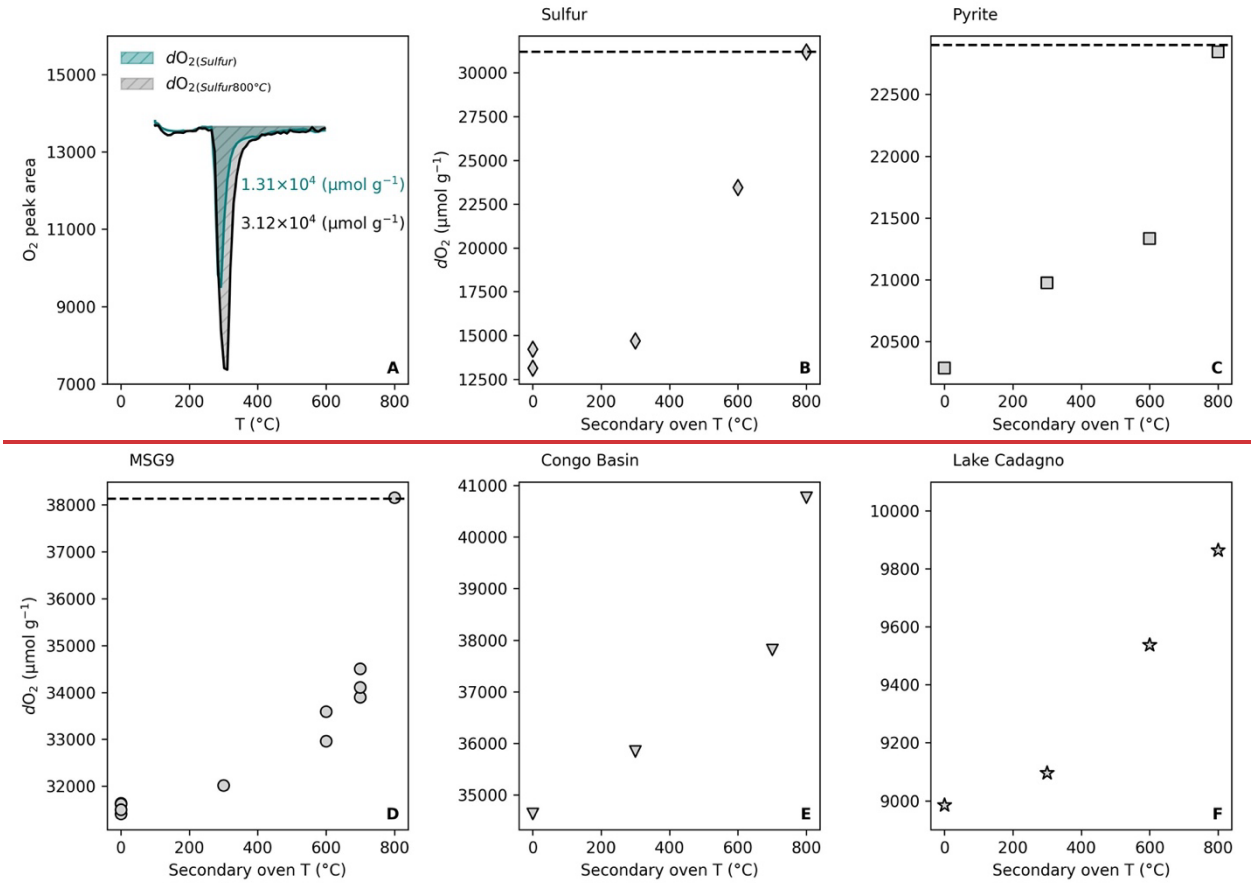
Sulfur
Pyrite
MSG9
Congo Basin
Lake Cadagno
$dO_{2(Sulfur)}$
$dO_{2(Sulfur800°C)}$
1.31×10^4 (µmol g^{-1})
3.12×10^4 (µmol g^{-1})
O_2 peak area
dO_2 (µmol g^{-1})
T (°C)
Secondary oven T (°C)
A
B
C
D
E
F

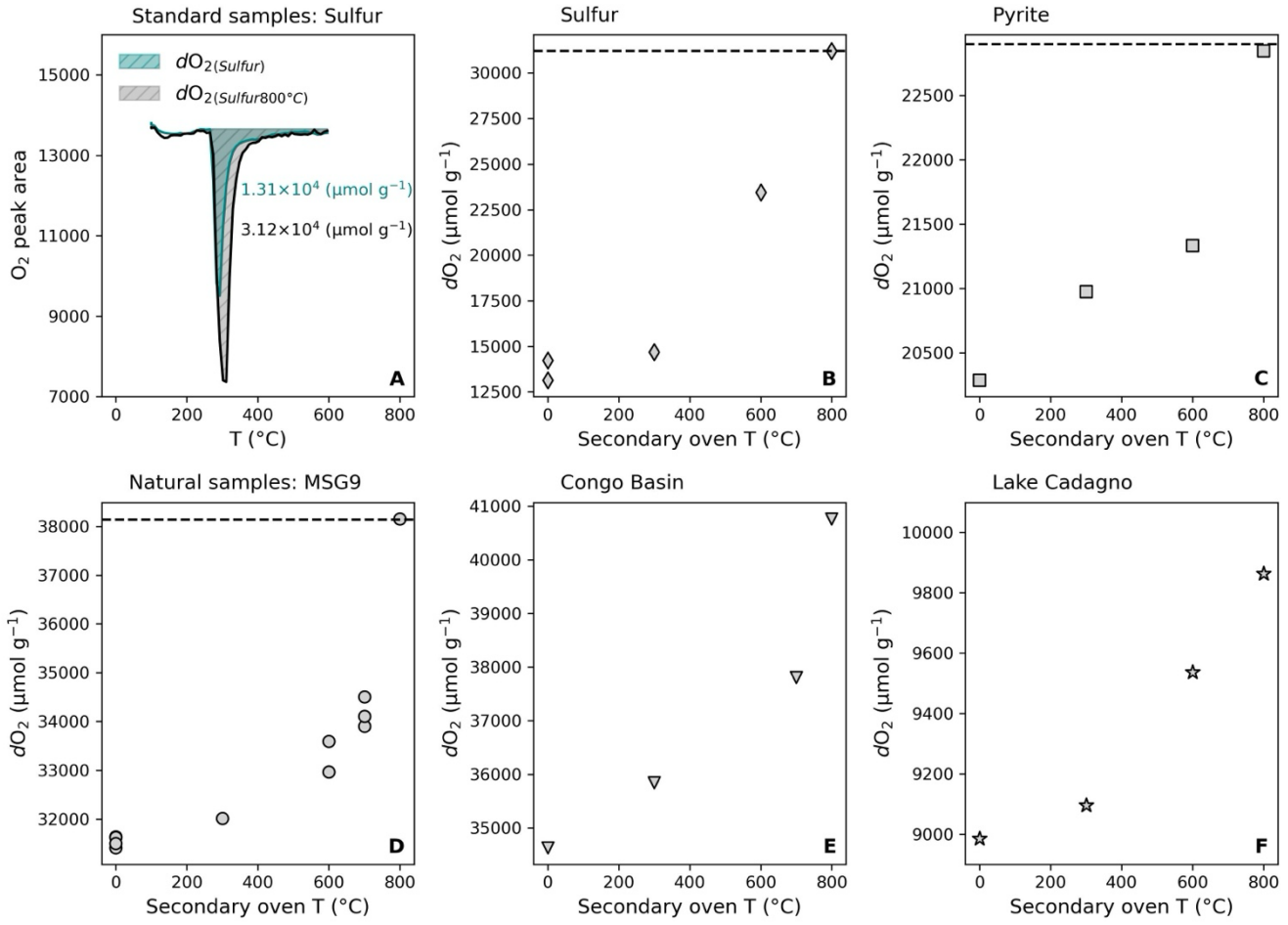

Figure 7. Optimized redox capacity with secondary oven. A, Comparison of elemental sulfur measurements with secondary oven (at 800°C, grey) and without secondary oven (teal); **B**, Elemental sulfur; **C**, Pyrite; **D**, Black shale (MSG9); **E**, Peat sediment from the Congo basin; **F**, Lake Cadagno sediment. Black dashed lines in B, C and D panels indicate the theoretical values.

4 Kinetic fingerprints

4.1 Oxygen consumption and redox-active components

Beyond quantifying total redox capacity, our approach yields kinetically resolved oxygen consumption profiles, ~~offering~~ providing a distinctive ~~"~~redox fingerprint~~"~~ of ~~reducible components~~natural materials. The Congo Basin sample exhibits a ~~dual~~ bimodal oxidation pattern: ~3~~76.9~~% of the total O_2 ~~attributed~~ corresponds to ~~labile organic matter~~a low-temperature fraction oxidized~~ing~~ in the~~at~~ 250–450 °C window, consistent with labile organic matter, ~~while~~ whereas the dominant fraction (63.1%) is associated with a higher-temperature fraction oxidized about 500°C, consistent with more refractory organic matter ~~oxidizeding above 500 °C~~ (Fig. 8A). These two oxidation stages are ~~consistent~~ supported with broad CO_2 peaks observed in the gas evolution data (Fig. 8D)~~, confirming the contrasting thermal stability of organic matter pools~~.

The Lake Cadagno sediment exhibits a mixed organic C–S oxidation signature, with 38.0% of ~~the~~ total O_2 uptake ~~derived from organic~~associated with low-temperature C and S-bearing compounds, and 62.0% associated with higher-temperature oxidation of refractory ~~C~~ carbon and pyrite oxidation~~,~~ extending to ~700 °C (Fig. 8B). The ~~synchronous~~ coupled evolution of CO_2, SO_2, COS and ~~,~~H_2S (Fig. 8E)~~,~~ reflects ~~coupled~~ the co-occurrence ~~oxidation~~ of sulfurized organic matter and pyrite, ~~highlighting~~ consistent with microbially mediated sulfurization of buried organic matter and pyrite formation under euxinic conditions ~~and its long-term preservation in the sedimentary record~~.

In contrast, the fayalite standard is dominated by Fe(II) oxidation, which accounts for 88.1% of the total O_2 consumption at high temperatures (500-900°C), with only 11.9% ~~originates~~ ~~originating~~attributed ~~from~~ to minor low-temperature organic matter oxidation (Fig. 8C). This interpretation is consistent with a weak low-temperature CO_2 peak and illustrates the method's ability to distinguish metal-driven versus organic- and sulfur driven redox ~~processes~~ carriers (Fig. 8C, F).

Together, these results demonstrate that integrating O_2 consumption profile with simultaneous gas evolution measurements enables the semi-quantitative partitioning of oxygen demand among labile organic matter, refractory carbon, sulfur-bearing phases, and Fe(II) minerals. This~~,~~ provides~~ing~~ a ~~comprehensive~~ kinetically resolved redox characterization of ~~the thermal reactivity of~~ sediments and minerals that cannot be obtained from bulk elemental composition alone.~~.~~

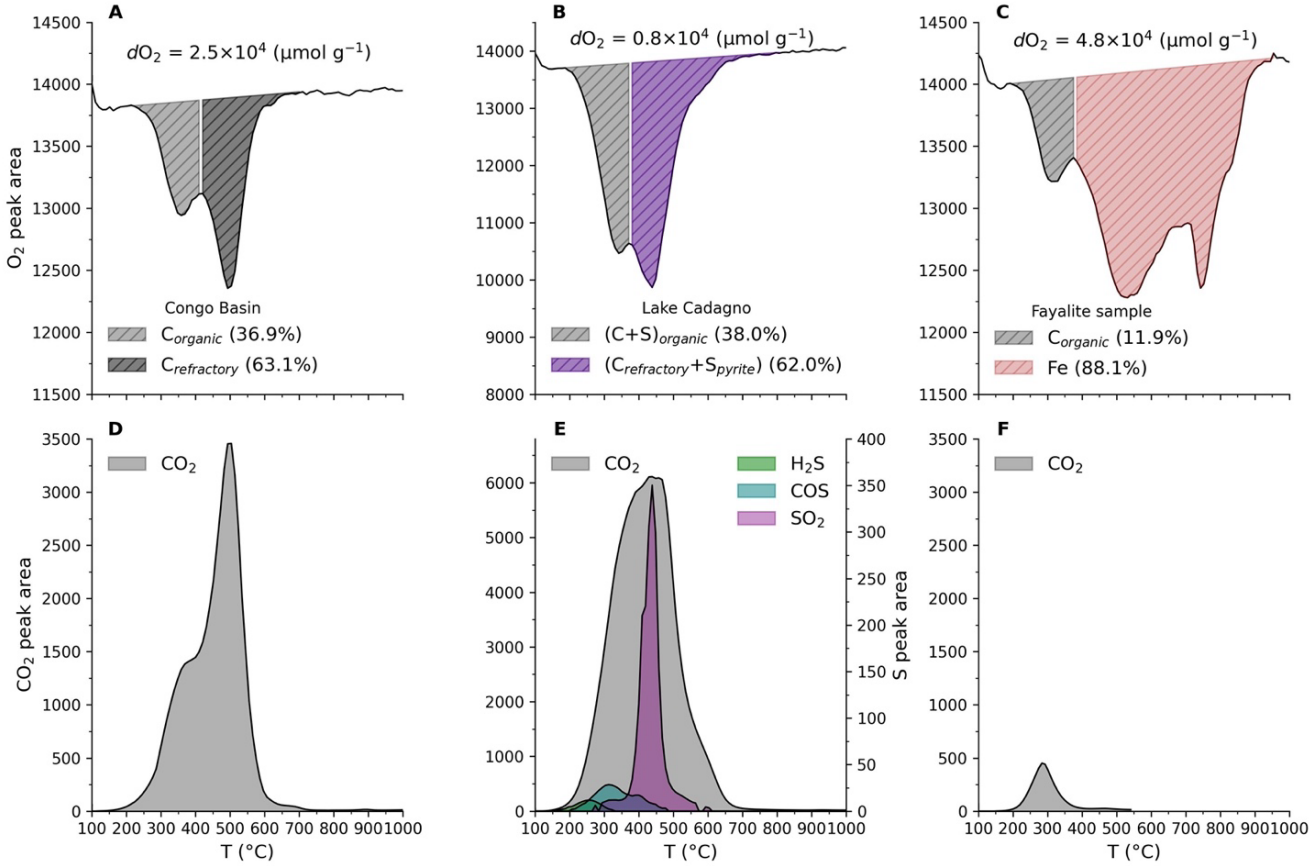

Figure 8. Oxidation profile with corresponding components. A, Congo Basin peat sample; **B**, Cadagno Lake sediment sample; **C**, Fayalite sample; **D-F**, Gases released through distinct reactions from samples A, B and C, respectively.

4.2 Sulfur cycle and dDiagenesis in Lake Cadagno Lake

To further demonstrate the capabilities of our method, we applied it to a sediment profile from Lake Cadagno, a well-known system for studying microbial sulfur cycling and diagenetic processes (Berg et al., 2022; Berg et al., 2025; Dupeyron et al., 2025).

Our results reveal a distinct redox transition marked by a progressive decline in dO_2 and total organic carbon (TOC) with depth, while COS and H_2S signals persist throughout the profile (Fig. 9A-D). In contrast, SO_2 concentrations release during analysis are low near the surface, increases sharply to a maximum around 18-20 cm, and then declines toward to the base of the core (Fig. 9E). This hump-shaped SO_2 pattern identifies suggests a zone of intense S remobilization and re-oxidation, coinciding with the microbial redox transition zone where in which sulfate reduction peaksand sulfide mineral formation were particularly active.

The aE_a spectra, derived from the SO_2 release kinetics, provide a deeper view into the progression of S diagenesis. In the upper zone (7-15 cm), the spectra exhibit multiple peaks spanning 80-240 kJ mol^{-1}, reflecting consistent with a heterogeneous assemblage of metastable metal sulfides, including labile and metastable reduced-S phases, including poorly crystalline (such ase.g. Fe monoo-nsulfides and trace metal sulfides ZnS, $Fe_{1-x}S$, and PbS (, (Fig. 9F). In the transitional middle zone (15-19 cm), the spectra simplify to three partially overlapping peaks, indicating progressive loss of the most labile sulfide phases and their partial transformation into more stable S-bearing minerals (Fig. 9G). Below the 19-20 cm boundary, the spectra converge into a single dominant peak at approximately 140-160 kJ mol^{-1}, consistent with the formation predominance of tmore thermally stable pyrite (FeS_2) (Fig. 9H). This clear diagenetic transition from diverse assemblage of, reactive sulfides to a single,more

uniform and thermally stable phase~~s~~ of pyrite highlights the multi-stage and progressive nature of sulfur mineral maturation in anoxic sediments.

We interpret the 19-20 cm boundary as marking a sulfate-depletion front, consistent with recent study (Dupeyron et al., 2025)~~., where organic matter driven sulfate reduction in the upper sediment generates H_2S that precipitating transient metal sulfides, while deeper layers record the maturation of pyrite sustained by internal sulfur cycling under sulfate limited conditions.~~ The transformation into stable pyrite is consistent with a ~~strengthens the long-term sulfur burial and~~ reduction in~~es~~ the pool of reactive sulfur species and progressive sulfur mineral maturation with depth~~, potentially modulating redox balance, microbial metabolism and biodiversity in meromictic lake systems~~. By resolving activation--energy distributions, our method provides a new kinetic framework for tracking diagenetic fronts and reconstructing microbial sulfur cycling and redox transitions in anoxic environments. ~~, offering a powerful tool for paleoenvironmental and early diagenetic studies.~~

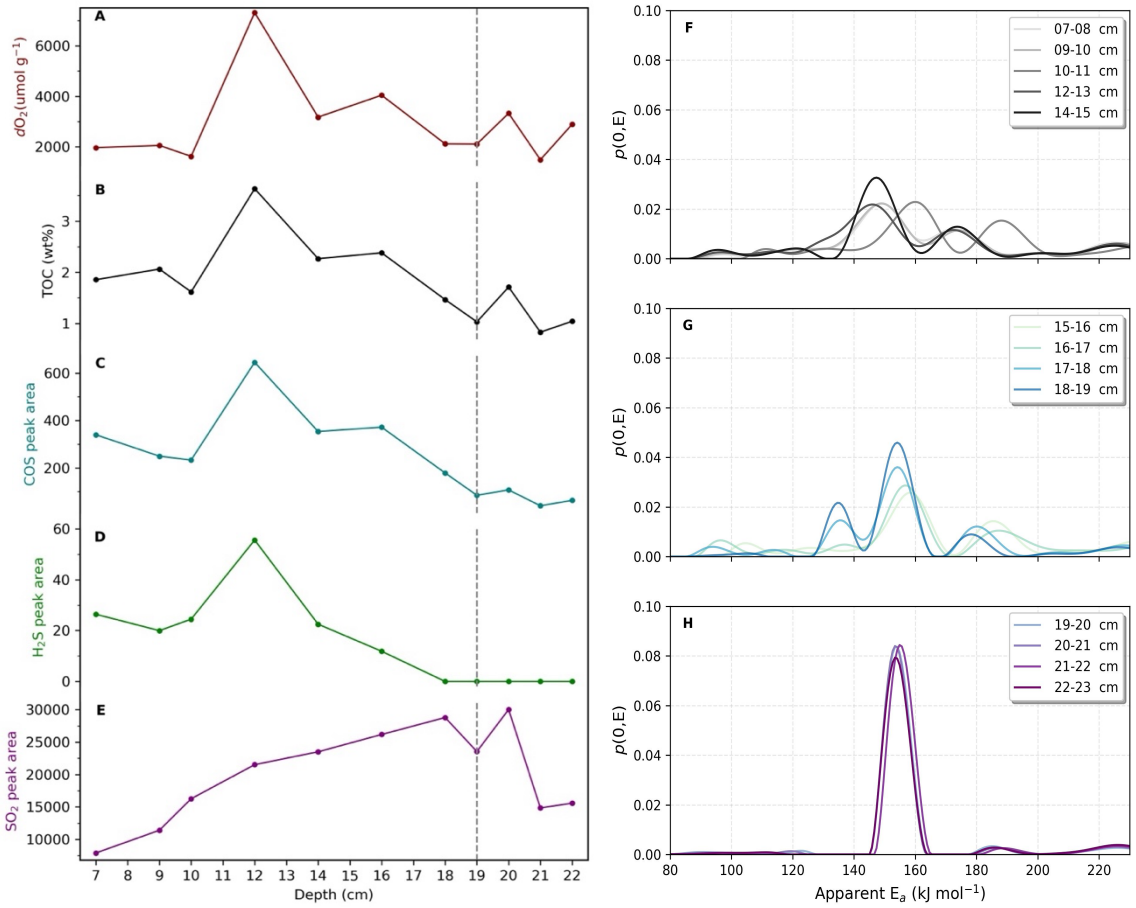

480 **Figure 9. Cadagno Lake depth profile. A**, dO_2; **B**, TOC content; **C**, COS; **D**, H_2S; **E**, SO_2; **F**, aE_a spectral distributions of SO_2 from the upper zone (7-15 cm); **G**, aE_a spectral distributions of SO_2 from the middle zone (15-19 cm). **H**, aE_a spectral distributions of SO_2 from the lower zone (19-22 cm). Dash line indicates the diagenetic boundary.

485

4.3 Kinetic fingerprint ~~for~~ of materials: redox chemistry

The TGA/DSC-MicroGC platform delivers a comprehensive~~unified~~ combustion kinetic fingerprint, that is, —a spectral signature of H, C, O~~S~~, ~~O, and H reactivity~~and S reactivity, —captured in a single analytical run under controlled ramped oxidation. ~~This kinetic fingerprint is exemplified in~~ Fig. 10 represents~~is~~ the kinetic fingerprint for a representative sulfidic sediment from Lake Cadagno. It shows ~~gradual~~ the progressive sample mass loss and the corresponding heat--flow profile, ~~where~~ which together ~~exothermic features highlight bond cleavage and oxidation reactions~~reflect oxidation reactions and associated bond transformations (Fig. 10A, B). Moreover, it tracks the oxidation-consumption profile and the evolution of diagnostic~~ved~~ gases, , ~~revealing O_2 consumption alongside reduced components,~~ including ~~organic~~ C- and ~~mineral sulfur species and carbon~~S-bearing species (~~H_2S,~~CO_2, COS, SO_2 and ~~CO_2~~H_2S) (Fig. 10C, D and E). ~~Last but not least, t~~The apparent activation energy distributions ~~shows~~ further resolve the thermal reactivity of these phases. L~~l~~ow aE_a (~100–140 kJ mol^{-1}) ~~for~~ associated with H_2S and ~~,~~COS evolution, are consistent with thermally ~~indicating~~ labile organic ~~sulfur~~S-bearing compounds, including sulfurized organic matter and/or, metastable ~~mono~~sulfide phases~~s~~ ~~and~~ as well as more labile carbon pools carbon. ~~,~~ ~~while~~ In contrast high aE_a (~150–180 kJ mol^{-1}) ~~for~~ associated with SO_2 and~~,~~ CO_2 evolution ~~reflecting~~ are consistent with the oxidation of more refractory phases, including pyrite and thermally stable carbon (Fig. 10F).

By synchronously resolving mass-loss kinetics, enthalpic transitions, activation--energy distributions, and near-continuous evolved gas profiles ~~(O_2, CO_2, H_2S, COS, SO_2)~~ (Fig. 10), this approach provides a kinetically resolved characterization of redox-active phases. It~~,~~ links~~ing~~ thermal stability, gas evolution and oxygen demand within a

unified analytical framework. ~~this approach resolves the molecular identity, thermal stability, and redox~~

510 ~~stoichiometry of every electron-transferring phase.~~

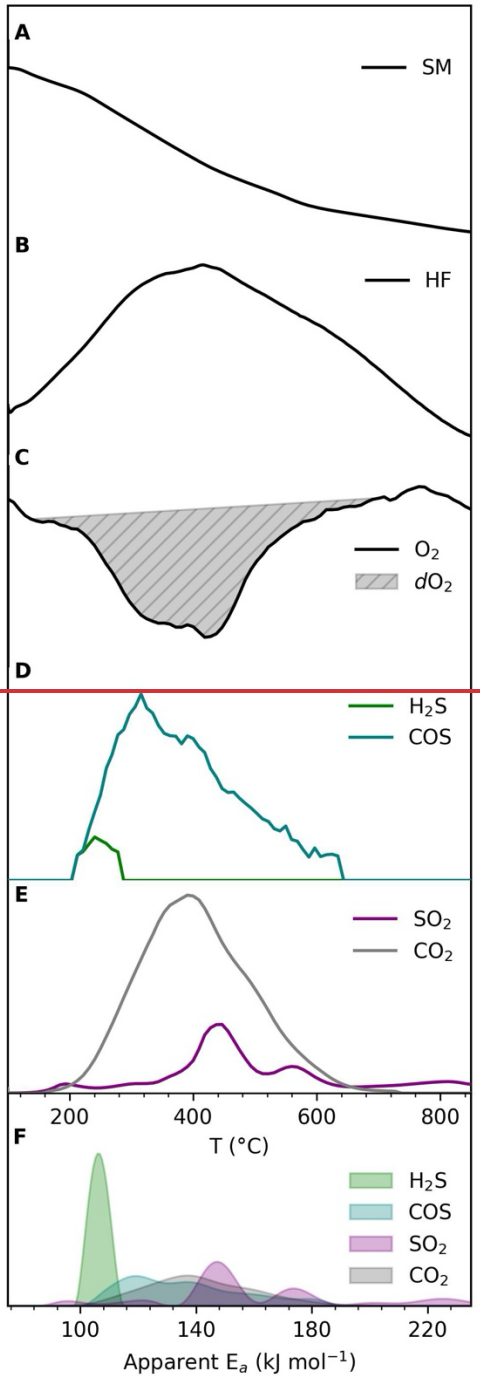
A
SM
B
HF
C
O_2
dO_2
D
H_2S
COS
E
SO_2
CO_2
200
400
600
800
T (°C)
F
H_2S
COS
SO_2
CO_2
100
140
180
220
Apparent E_a (kJ mol^{-1})

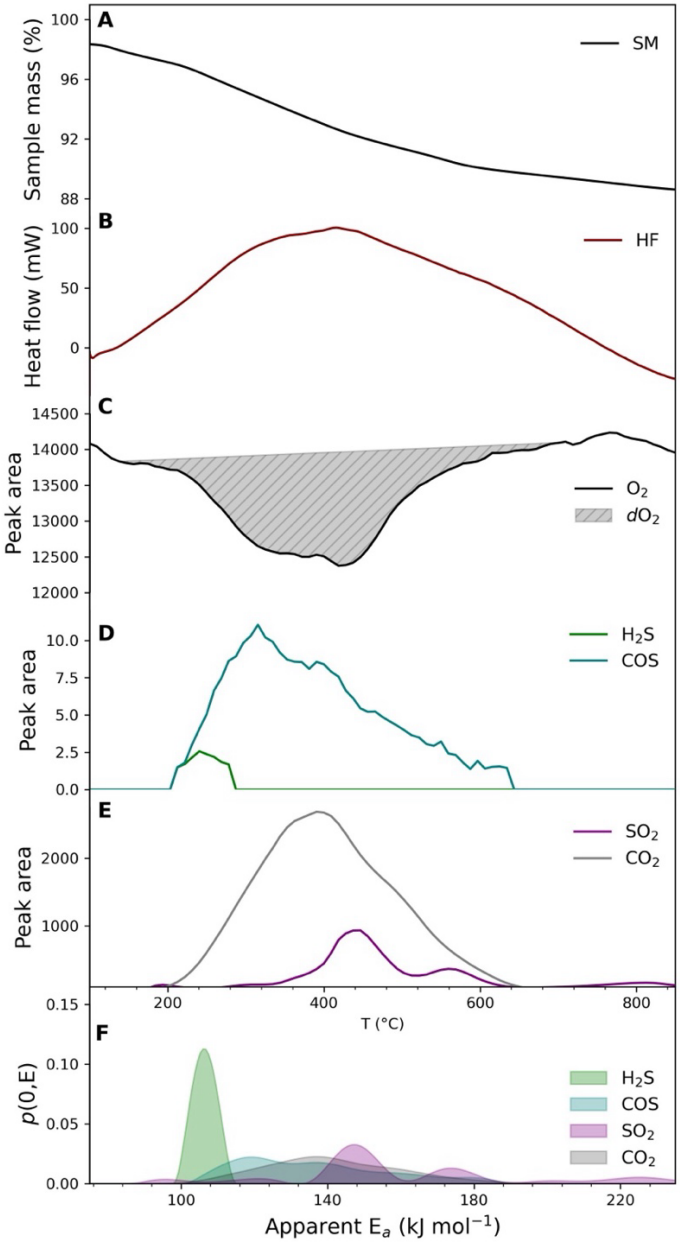

Figure 10. Kinetic fingerprint for a representative sulfidic sediment from Lake Cadagno. A, Sample mass (SM) changes at heating rates of 10°C min^{-1}; **B**, Heat flow (HF) profile; **C**, Oxidation profile; **D,** H_2S and COS profiles; **E**, SO_2 and CO_2 profiles; **F**, aE_a distribution of H_2S, COS, SO_2 and CO_2.

5 Conclusions

In this study, we ~~have have developed and validated~~presented a novel, integrated TGA/DSC-MicroGC analytical system that enables kinetically resolved characterization of ~~thermal decomposition, evolved gas composition and oxidation profiles during controlled thermal oxidation offers unprecedented resolution of biogeochemical speciation and reactivity in~~ geological materials using high-resolution thermal analysis. By combining thermogravimetric analysis, differential scanning calorimetry~~,~~ and ultra-fast gas chromatography within a single experimental framework, t~~T~~his method provides a mechanistic approach for distinguishing ~~kinetically resolves the thermal decomposition of~~ complex ~~carbon~~C- and ~~sulfur~~S-bearing ~~C and S species~~reactive pools based on their thermal reactivity and gas-evolution signature~~thermal reactions and activation energy distribution~~ It ~~, while~~ also ~~quantif~~quantifies~~ying~~ ~~absolute~~total and fractional redox capacity (*oxidability*) through ~~continuous~~timeresolved monitoring of oxygen demand during controlled ramped oxidation~~,~~. These ~~capabilities on~~insights about elemental speciation, reaction kinetics, and redox ~~behavior that~~ signature cannot be resolved using conventional bulk analyses alone~~inaccessible to conventional bulk analyses, while also enabling the quantification of absolute redox capacity and continuous kinetically resolved oxidation profiles.~~.

Applications to natural archives from the Congo Basin and Lake Cadagno demonstrate the method's broad utility and ~~transformative implications~~environmental ~~applications~~relevance. In ~~tropical~~ Congo Basin peatland sediments, the method differentiated t~~T~~hermally labile and refractory organic carbon pools and quantifies their contrasting oxygen demand, providing a new framework for tracing changes in organic matter preservation and~~it allowed the quantification of paleo-oxygen fluxes linked to organic C burial~~ ~~paleo-oxygen~~paleoenvionmental ~~fluxes~~redox dynamics (Galvez et al., 2025). In Lake Cadagno sediments, our results ~~revealed~~ reveal a diagenetic front defined by a shift in sulfide speciation and apparent activation~~-~~energy, providing a direct kinetic proxy for past microbial

~~processes~~ S cycling and redox evolution. More broadly, the integration of oxygen consumption profiles with evolved gas signatures allows semi-quantitative partitioning of redox-active components among organic matter, sulfur-bearing phases, and Fe-bearing minerals, yielding a kinetic "redox fingerprint" of geological materials.

Overall, this integrated approach moves beyond static compositional~~bulk~~ measurements toward a mechanistic, high-resolution framework for tracing coupled C-O-S dynamics in Earth materials. The TGA/DSC-MicroGC platform provides a versatile tool for investigating redox conditions, paleoenvironmental change, and biogeochemical reactivity across diverse natural systems. Future applications to marine sediments, soils, and ancient rock archives may further refine our understanding of redox processes across environmental settings and their links to elemental cycling and Earth evolution.~~Future application to rocks, marine sediment, soils, meteorites, and other anoxic environments promise to advance our understanding of the co-evolution of life, climate and planetary redox balance.~~

Data availability

The data related to this study will be openly available in Zenodo.

Author contributions

Conceptualization: M.E.G.~~, S.W.~~; Investigation: S.W., M.E.G.; Methodology: S.W., M.E.G. Writing – original draft: S.W.; Writing – review and editing: S.W., S.L.J., M.E.G.

Competing interests

The authors declare no competing financial interest.

Acknowledgements

~~This project was supported through Swiss National Science Foundation grant 215097 (M.E.G.).~~ We thank J. Dupeyron, J. Marin~~.~~ Carbonne and Y. Garcin for proving the sediment samples from the Lake Cadagno and the Congo Basin as well as for their helpful discussions. S. W acknowledges funds from the Chinese Academy of Sciences-Pioneer Hundred Talents Program (grant E5710403). This study was supported by ~~Funding from~~ the Swiss National Science Foundation ~~is acknowledged~~ (grant 215097 to M.E.G. and grants 200021_163003 and 200020_192361 awarded to S.L.J.).

References

Alt, J. C. and Shanks Iii, W. C.: Stable isotope compositions of serpentinite seamounts in the Mariana forearc: Serpentinization processes, fluid sources and sulfur metasomatism, Earth Planet Sc Lett, 242, 272–285, 10.1016/j.epsl.2005.11.063, 2006.

Berg, J. S., Rodriguez, P. C., Magnabosco, C., Deng, L., Bernasconi, S. M., Vogel, H., Morlock, M., and Lever, M. A.: Active microbial sulfur cycling across a 13,500-year-old lake sediment record, EGUsphere, 2025, 1–27, 10.5194/egusphere-2024-4158, 2025.

Berg, J. S., Lepine, M., Laymand, E., Han, X., Vogel, H., Morlock, M. A., Gajendra, N., Gilli, A., Bernasconi, S. M., Schubert, C. J., Su, G., and Lever, M. A.: Ancient and Modern Geochemical Signatures in the 13,500-Year Sedimentary Record of Lake Cadagno, Front Earth Sc-Switz, Volume 9 - 2021, 10.3389/feart.2021.754888, 2022.

Boudreau, B. P.: A kinetic model for microbic organic-matter decomposition in marine sediments, FEMS Microbiology Ecology, 11, 1–14, 10.1111/j.1574-6968.1992.tb05789.x, 1992.

Carter, T. L., Schaecher, C., Monteith, S., and Ferguson, R.: Using combustion analysis to simultaneously measure soil organic and inorganic carbon, GEODERMA, 451, 10.1016/j.geoderma.2024.117066, 2024.

Cohen-Sadon, H., Amrani, A., Feinstein, S., and Rosenberg, Y. O.: A new empirical approach for rapid quantification of organic and pyritic sulfur in sedimentary rocks using the Rock-Eval 7S, Organic Geochemistry, 166, 104350, 10.1016/j.orggeochem.2021.104350, 2022.

Crezee, B., Dargie, G. C., Ewango, C. E. N., Mitchard, E. T. A., Emba B, O., Kanyama T, J., Bola, P., Ndjango, J.-B. N., Girkin, N. T., Bocko, Y. E., Ifo, S. A., Hubau, W., Seidensticker, D., Batumike, R., Imani, G., Cuní-Sanchez, A., Kiahtipes, C. A., Lebamba, J., Wotzka, H.-P., Bean, H., Baker, T. R., Baird, A. J., Boom, A., Morris, P. J., Page, S. E., Lawson, I. T., and Lewis, S. L.: Mapping peat thickness and carbon stocks of the central Congo Basin using field data, Nat Geosci, 15, 639–644, 10.1038/s41561-022-00966-7, 2022.

Dupeyron, J., Pasquier, V., Guibourdenche, L., Busigny, V., Cartigny, P., Jézéquel, D., Bernasconi, S. M., and Carbonne, J. M.: Decadal, sediment-driven sulfur isotope evolution in Lake Cadagno, Geochemical Perspectives Letters, 38, 17–22, 10.7185/geochemlet.2550, 2025.

Espitalie, J., Deroo, G., and Marquis, F.: Rock-Eval Pyrolysis and Its Applications (Part Two), Rev. Inst. Fr. Pét., 40, 755–784, 10.2516/ogst:1985045, 1985.

Galvez, M., Wu, S., Garcin, Y., Schefuß, E., Gassier, G., Lebamba, J., Kiahtipes, C., Bokomba, F., Wotzka, H. P., and Adatte, T.: Peatlands' O_2 Pulses: Time-resolved Terrestrial Oxygen Production in the Central Congo Basin over the Holocene, Nature Geoscience (under review), 10.21203/rs.3.rs-7398366/v1, 2026.

Galvez, M. E.: Redox constraints on a Cenozoic imbalance in the organic carbon cycle, American Journal of Science, 320, 730–751, 10.2475/10.2020.03, 2020.

Galvez, M. E. and Jaccard, S. L.: Redox capacity of rocks and sediments by high temperature chalcometric titration, Chemical Geology, 564, 120016, 10.1016/j.chemgeo.2020.120016, 2021.

Galvez, M. E., Müntener, O., and Jaccard, S. L.: Beyond Oxygen Fugacity: A Compositional Metric to Probe Earth's Redox Structure, Geophys Res Lett, 52, e2025GL117642, 10.1029/2025GL117642, 2025.

Galvez, M. E., Fischer, W. W., Jaccard, S. L., and Eglinton, T. I.: Materials and pathways of the organic carbon cycle through time, Nat Geosci, 13, 535–546, 10.1038/s41561-020-0563-8, 2020.

Garcin, Y., Schefuß, E., Dargie, G. C., Hawthorne, D., Lawson, I. T., Sebag, D., Biddulph, G. E., Crezee, B., Bocko, Y. E., Ifo, S. A., Mampouya Wenina, Y. E., Mbemba, M., Ewango, C. E. N., Emba, O., Bola, P., Kanyama Tabu, J., Tyrrell, G., Young, D. M., Gassier, G., Girkin, N. T., Vane, C. H., Adatte, T., Baird, A. J., Boom, A., Gulliver, P., Morris, P. J., Page, S. E., Sjögersten, S., and Lewis, S. L.: Hydroclimatic vulnerability of peat carbon in the central Congo Basin, Nature, 612, 277–282, 10.1038/s41586-022-05389-3, 2022.

Hayes, J. M. and Waldbauer, J. R.: The carbon cycle and associated redox processes through time, Philosophical Transactions of the Royal Society B: Biological Sciences, 361, 931–950, 10.1098/rstb.2006.1840, 2006.

Hemingway, J. D., Rothman, D. H., Rosengard, S. Z., and Galy, V. V.: Technical note: An inverse method to relate organic carbon reactivity to isotope composition from serial oxidation, Biogeosciences, 14, 5099–5114, 10.5194/bg-14-5099-2017, 2017.

Hemingway, J. D., Hilton, R. G., Hovius, N., Eglinton, T. I., Haghipour, N., Wacker, L., Chen, M.-C., and Galy, V. V.: Microbial oxidation of lithospheric organic carbon in rapidly eroding tropical mountain soils, Science, 360, 209–212, 10.1126/science.aao6463, 2018.

Janssen, D. J., Rickli, J., Wille, M., Sepúlveda Steiner, O., Vogel, H., Dellwig, O., Berg, J. S., Bouffard, D., Lever, M. A., Hassler, C. S., and Jaccard, S. L.: Chromium Cycling in Redox-Stratified Basins Challenges δ53Cr Paleoredox Proxy Applications, Geophys Res Lett, 49, e2022GL099154, 10.1029/2022GL099154, 2022.

L'Vov, B. V.: Mechanism of thermal decomposition of alkaline-earth carbonates, Thermochimica Acta, 303, 161–170, 10.1016/S0040-6031(97)00261-X, 1997.

Ordoñez, L., Vogel, H., Sebag, D., Ariztegui, D., Adatte, T., Russell, J. M., Kallmeyer, J., Vuillemin, A., Friese, A., Crowe, S. A., Bauer, K. W., Simister, R., Henny, C., Nomosatryo, S., and Bijaksana, S.: Empowering conventional Rock-Eval pyrolysis for organic matter characterization of the siderite-rich sediments of Lake Towuti (Indonesia) using End-Member Analysis, Organic Geochemistry, 134, 32–44, 10.1016/j.orggeochem.2019.05.002, 2019.

Paytan, A., Kastner, M., Campbell, D., and Thiemens, M. H.: Sulfur Isotopic Composition of Cenozoic Seawater Sulfate, Science, 282, 1459–1462, 10.1126/science.282.5393.1459, 1998.

Salonen, K.: A versatile method for the rapid and accurate determination ofcarbon by high temperature combustion, LIMNOLOGY AND OCEANOGRAPHY, 24, 177–183, 10.4319/lo.1979.24.1.0177, 1979.

Sebag, D., Verrecchia, E. P., Cécillon, L., Adatte, T., Albrecht, R., Aubert, M., Bureau, F., Cailleau, G., Copard, Y., Decaens, T., Disnar, J. R., Hetényi, M., Nyilas, T., and Trombino, L.: Dynamics of soil organic matter based on new Rock-Eval indices, Geoderma, 284, 185–203, 10.1016/j.geoderma.2016.08.025, 2016.

Vyazovkin, S. and Wight, C. A.: Model-free and model-fitting approaches to kinetic analysis of isothermal and nonisothermal data, Thermochimica Acta, 340-341, 53–68, 10.1016/S0040-6031(99)00253-1, 1999.

Yoon, G., Park, S.-M., Yang, H., Tsang, D. C. W., Alessi, D. S., and Baek, K.: Selection criteria for oxidation method in total organic carbon measurement, Chemosphere, 199, 453–458, 10.1016/j.chemosphere.2018.02.074, 2018.

Zhao, W. Z., Lu, B., Lv, S. N., Zhou, C. F., and Yang, Y.: Simultaneous determination of chlorine and sulfur in geochemical reference samples by wavelength dispersive X-ray fluorescence spectrometry, NEW JOURNAL OF CHEMISTRY, 44, 11224–11230, 10.1039/d0nj02042g, 2020.

Alt, J. C. and Shanks Iii, W. C.: Stable isotope compositions of serpentinite seamounts in the Mariana forearc: Serpentinization processes, fluid sources and sulfur metasomatism, Earth Planet Sc Lett, 242, 272–285, 10.1016/j.epsl.2005.11.063, 2006.

Berg, J. S., Rodriguez, P. C., Magnabosco, C., Deng, L., Bernasconi, S. M., Vogel, H., Morlock, M., and Lever, M. A.: Active microbial sulfur cycling across a 13,500-year-old lake sediment record, EGUsphere, 2025, 1–27, 10.5194/egusphere-2024-4158, 2025.

Berg, J. S., Lepine, M., Laymand, E., Han, X., Vogel, H., Morlock, M. A., Gajendra, N., Gilli, A., Bernasconi, S. M., Schubert, C. J., Su, G., and Lever, M. A.: Ancient and Modern Geochemical Signatures in the 13,500-Year Sedimentary Record of Lake Cadagno, Front Earth Sc-Switz, Volume 9 - 2021, 10.3389/feart.2021.754888, 2022.

Boudreau, B. P.: A kinetic model for microbic organic-matter decomposition in marine sediments, FEMS Microbiology Ecology, 11, 1–14, 10.1111/j.1574-6968.1992.tb05789.x, 1992.

Carter, T. L., Schaecher, C., Monteith, S., and Ferguson, R.: Using combustion analysis to simultaneously measure soil organic and inorganic carbon, GEODERMA, 451, 10.1016/j.geoderma.2024.117066, 2024.

Cohen-Sadon, H., Amrani, A., Feinstein, S., and Rosenberg, Y. O.: A new empirical approach for rapid quantification of organic and pyritic sulfur in sedimentary rocks using the Rock-Eval 7S, Organic Geochemistry, 166, 104350, 10.1016/j.orggeochem.2021.104350, 2022.

Crezee, B., Dargie, G. C., Ewango, C. E. N., Mitchard, E. T. A., Emba B, O., Kanyama T, J., Bola, P., Ndjango, J. B. N., Girkin, N. T., Bocko, Y. E., Ifo, S. A., Hubau, W., Seidensticker, D., Batumike, R., Imani, G., Cuní-Sanchez, A., Kiahtipes, C. A., Lebamba, J., Wotzka, H. P., Bean, H., Baker, T. R., Baird, A. J., Boom, A., Morris, P. J., Page, S. E., Lawson, I. T., and Lewis, S. L.: Mapping peat thickness and carbon stocks of the central Congo Basin using field data, Nat Geosci, 15, 639–644, 10.1038/s41561-022-00966-7, 2022.

Dupeyron, J., Pasquier, V., Guibourdenche, L., Busigny, V., Cartigny, P., Jézéquel, D., Bernasconi, S. M., and Carbonne, J. M.: Decadal, sediment-driven sulfur isotope evolution in Lake Cadagno, Geochemical Perspectives Letters, 38, 17–22, 10.7185/geochemlet.2550, 2025.

Espitalie, J., Deroo, G., and Marquis, F.: Rock-Eval Pyrolysis and Its Applications (Part Two), Rev. Inst. Fr. Pét., 40, 755–784, 10.2516/ogst:1985045, 1985.

Galvez, M., Wu, S., Garcin, Y., Schefuß, E., Gassier, G., Lebamba, J., Kiahtipes, C., Bokomba, F., Wotzka, H. P., and Adatte, T.: Peatlands' O_2 Pulses: Time-resolved Terrestrial Oxygen Production in the Central Congo Basin over the Holocene, Nature Geoscience (under review), 10.21203/rs.3.rs-7398366/v1, 2025.

Galvez, M. E.: Redox constraints on a Cenozoic imbalance in the organic carbon cycle, American Journal of Science, 320, 730–751, 10.2475/10.2020.03, 2020.

Galvez, M. E. and Jaccard, S. L.: Redox capacity of rocks and sediments by high temperature chalcometric titration, Chemical Geology, 564, 120016, 10.1016/j.chemgeo.2020.120016, 2021.

Galvez, M. E., Fischer, W. W., Jaccard, S. L., and Eglinton, T. I.: Materials and pathways of the organic carbon cycle through time, Nat Geosci, 13, 535–546, 10.1038/s41561-020-0563-8, 2020.

Garcin, Y., Schefuß, E., Dargie, G. C., Hawthorne, D., Lawson, I. T., Sebag, D., Biddulph, G. E., Crezee, B., Bocko, Y. E., Ifo, S. A., Mampouya Wenina, Y. E., Mbemba, M., Ewango, C. E. N., Emba, O., Bola, P., Kanyama Tabu, J., Tyrrell, G., Young, D. M., Gassier, G., Girkin, N. T., Vane, C. H., Adatte, T., Baird, A. J., Boom, A., Gulliver, P., Morris, P. J., Page, S. E., Sjögersten, S., and Lewis, S. L.: Hydroclimatic vulnerability of peat carbon in the central Congo Basin, Nature, 612, 277–282, 10.1038/s41586-022-05389-3, 2022.

Hayes, J. M. and Waldbauer, J. R.: The carbon cycle and associated redox processes through time, Philosophical Transactions of the Royal Society B: Biological Sciences, 361, 931–950, 10.1098/rstb.2006.1840, 2006.

Hemingway, J. D., Rothman, D. H., Rosengard, S. Z., and Galy, V. V.: Technical note: An inverse method to relate organic carbon reactivity to isotope composition from serial oxidation, Biogeosciences, 14, 5099–5114, 10.5194/bg-14-5099-2017, 2017.

Hemingway, J. D., Hilton, R. G., Hovius, N., Eglinton, T. I., Haghipour, N., Wacker, L., Chen, M. C., and Galy, V. V.: Microbial oxidation of lithospheric organic carbon in rapidly eroding tropical mountain soils, Science, 360, 209–212, 10.1126/science.aao6463, 2018.

Janssen, D. J., Rickli, J., Wille, M., Sepúlveda Steiner, O., Vogel, H., Dellwig, O., Berg, J. S., Bouffard, D., Lever, M. A., Hassler, C. S., and Jaccard, S. L.: Chromium Cycling in Redox-Stratified Basins Challenges δ53Cr Paleoredox Proxy Applications, Geophys Res Lett, 49, e2022GL099154, 10.1029/2022GL099154, 2022.

L'Vov, B. V.: Mechanism of thermal decomposition of alkaline-earth carbonates, Thermochimica Acta, 303, 161–170, 10.1016/S0040-6031(97)00261-X, 1997.

Ordoñez, L., Vogel, H., Sebag, D., Ariztegui, D., Adatte, T., Russell, J. M., Kallmeyer, J., Vuillemin, A., Friese, A., Crowe, S. A., Bauer, K. W., Simister, R., Henny, C., Nomosatryo, S., and Bijaksana, S.: Empowering conventional Rock-Eval pyrolysis for organic matter characterization of the siderite-rich sediments of Lake Towuti (Indonesia) using End-Member Analysis, Organic Geochemistry, 134, 32–44, 10.1016/j.orggeochem.2019.05.002, 2019.

Paytan, A., Kastner, M., Campbell, D., and Thiemens, M. H.: Sulfur Isotopic Composition of Cenozoic Seawater Sulfate, Science, 282, 1459–1462, 10.1126/science.282.5393.1459, 1998.

Salonen, K.: A versatile method for the rapid and accurate determination ofcarbon by high temperature combustion, LIMNOLOGY AND OCEANOGRAPHY, 24, 177–183, 10.4319/lo.1979.24.1.0177, 1979.

Sebag, D., Verrecchia, E. P., Cécillon, L., Adatte, T., Albrecht, R., Aubert, M., Bureau, F., Cailleau, G., Copard, Y., Decaens, T., Disnar, J. R., Hetényi, M., Nyilas, T., and Trombino, L.: Dynamics of soil organic matter based on new Rock-Eval indices, Geoderma, 284, 185–203, 10.1016/j.geoderma.2016.08.025, 2016.

Vyazovkin, S. and Wight, C. A.: Model-free and model-fitting approaches to kinetic analysis of isothermal and nonisothermal data, Thermochimica Acta, 340-341, 53-68, 10.1016/S0040-6031(99)00253-1, 1999.

Yoon, G., Park, S. M., Yang, H., Tsang, D. C. W., Alessi, D. S., and Baek, K.: Selection criteria for oxidation method in total organic carbon measurement, Chemosphere, 199, 453-458, 10.1016/j.chemosphere.2018.02.074, 2018.

Zhao, W. Z., Lu, B., Lv, S. N., Zhou, C. F., and Yang, Y.: Simultaneous determination of chlorine and sulfur in geochemical reference samples by wavelength dispersive X-ray fluorescence spectrometry, NEW JOURNAL OF CHEMISTRY, 44, 11224-11230, 10.1039/d0nj02042g, 2020.